Supporting Information

Side-Arm Sterics Direct Conformation, Topology, and Function in Zirconium Metal–Organic Frameworks

S1. Materials

All the reagents and solvents used for the synthesis were commercially available from Sigma-Aldrich, Fisher Scientific, Ambeed, and used as received without further purification. Methyl 4-(cyanoacetyl)benzoate (≥95%), benzene-1,3,5-tricarboxaldehyde (97%), 2,5-dimethoxybenzene-1,4-dicarboxaldehyde (97%), isophthalaldehyde (97%), (4-bromobenzoyl)acetonitrile (97%), potassium hydroxide, ammonium acetate (≥98%), sodium nitrite (≥97%), diethylformamide (DEF, 99%), acetic acid (≥99%), ammonium hydroxide solution (28.0-30.0% NH_3 basis), and formic acid (95%) were obtained from Sigma-Aldrich. $ZrCl_4$ (>99.5%), *N,N*-dimethylformamide (DMF), hydrochloric acid (HCl) (36.5%~38%), tetrahydrofuran, acetone, and methanol were purchased from Fisher Scientific. 4-(2-Cyanoacetyl)benzoic acid (95%) was purchased from Ambeed.

S2. Experimental Methods

Physical measurements

^{1}H and ^{13}C NMR spectra were collected on a Bruker S4 Avance III 500 MHz system equipped with DCH CryoProbe and automated with a BACS-60 autosampler. $^{1}H-^{15}N$ heteronuclear single quantum coherence (HSQC and HMBC) NMR spectra were recorded on a Bruker Neo 600 MHz system w/ QCI-F cryoprobe. Scanning Electron Microscopy (SEM) images were collected using a Hitachi SU8030 FE-SEM (Dallas, TX) microscope at the EPIC/NUANCE facility at Northwestern University. Powder X-ray diffraction (PXRD) patterns were carried out on a STOESTADIMP powder diffractometer equipped with an asymmetric curved Germanium monochromator (Cu Kα1 radiation) and one-dimensional silicon strip detector (MYTHEN 1K from DECTRIS) at ambient temperature. The line focused Cu X-ray was operated at 40 kV and 40 mA. Powder samples were measured on a rotating holder in transmission mode. The N_2 isotherm was measured on a Tristar 3020 (Micromeritics) at 77 K, and the pore size distribution was calculated via Density Functional Theory (DFT) using a carbon slit pore model with a N_2 kernel. The Brunauer-Emmett-Teller (BET) surface area was determined within the region of P/P_0 = 0.005−0.1. Before N_2 isotherm measurement, the samples were activated by a similar supercritical carbon dioxide (SC-CO_2) drying method[1] except that acetone was used to exchange with CO_2. Thermogravimetric analysis (TGA) data were collected using a Netzsch STA 449 F3 Jupiter simultaneous thermal analysis (STA) instrument. Measurements were made under ultra-high purity N_2 gas flowing. Following a 10 minute isothermal step at 30 °C, the temperature was increased at a rate of 10 °C min^{-1} up to 1000 °C and held at that temperature in a final isothermal step for 10 minutes before cool down to 30 °C. The CO_2 and CH_4 adsorption experiment was performed with a Micromeritics ASAP 2020 surface area analyzer, and the temperature was maintained by using a Micromeritics Iso Controller. The H_2 uptake experiment was performed with a Micromeritics 3Flex multiport surface characterization equipped with enhanced chemical resistant analyzer.

Single-crystal X-ray diffraction measurement and analysis

The crystals were mounted on a MiTeGeN holder in Paratone oil on a XtaLAB Synergy R, DW system, HyPix diffractometer. The crystals C1, C2, C3, C4 (AM-Zr-1), and C5 (CN-Zr-1) were kept

at 166, 225, 250.00, 225.15, and 250.00 K during data collection, respectively. Using Olex2,[2] the structure was solved with the SHELXT[3] structure solution program using Dual Space for C2 and Intrinsic Phasing for the others and refined with the SHELXL[4] refinement package using Least Squares minimization. Disordered ring atoms are partially omitted for clarity in the Figures.

C1 refinement and solution treatment details: distance restraints were imposed on the disordered solvent molecule. The enhanced rigid-bond restraint (SHELX keyword RIGU) was also applied on the disordered solvent.[5] The solvent masking procedure as implemented in Olex2 was used to remove the electronic contribution of solvent molecules from the refinement. As the exact solvent content is not known, only the atoms used in the refinement model are reported in the formula here. Total solvent accessible volume/cell = 1422.8 Å^3 [25.3%] (solvate). Total electron count/cell = 363.9.

C2 refinement and solution treatment details: distance restraints were imposed on the rings to ensure it was chemically reasonable. Restraints on similar amplitudes on the disordered oxygen atom's displacement paramters were imposed (SHELX keyword SIMU). The enhanced rigid-bond restraint (SHELX keyword RIGU) was applied globally.[5] The solvent masking procedure as implemented in Olex2 was used to remove the electronic contribution of solvent molecules from the refinement. As the exact solvent content is not known, only the atoms used in the refinement model are reported in the formula here. Total solvent accessible volume/cell = 1108.2 Å^3 [25.3%] (solvate). Total electron count/cell = 327.5.

C3 refinement and solution treatment details: distance restraints were imposed on hydroxyl groups to ensure chemical reasonability. The solvent masking procedure as implemented in Olex2 was used to remove the electronic contribution of disordered solvent molecules from the refinement (acetic acid ordered in the pores was fitted). As the exact solvent content is not known, only the atoms used in the refinement model are reported in the formula here. Total solvent accessible volume/cell = 411 Å^3 + 13 Å^3. Total electron count/cell = 108 + 11.

C4 refinement and solution treatment details: the enhanced rigid-bond restraint (SHELX keyword RIGU) was applied on the disordered ring atoms.[5] The amide groups were restrained so that their Uij components approximate to isotropic. The solvent masking procedure as implemented in Olex2 was used to remove the electronic contribution of solvent molecules from the refinement. As the exact solvent content is not known, only the atoms used in the refinement model are reported in the formula here. Total solvent accessible volume/cell = 26394.0 Å^3 [71.2%]. Total electron count/cell = 4416.0.

C5 refinement and solution treatment details: distance restraints were imposed on the disordered atoms. The enhanced rigid-bond restraint (SHELX keyword RIGU) was applied on the disordered atoms as was restraints on similar amplitudes (SIMU) separated by less than 1.7 angstrom.[5] The solvent masking procedure as implemented in Olex2 was used to remove the electronic contribution of solvent molecules from the refinement. As the exact solvent content is not known, only the atoms used in the refinement model are reported in the formula here. Total solvent accessible volume/cell = 26858.3 Å^3 [70.8%]. Total electron count/cell = 7271.7.

S3. Computational Methods

Crystal structure refinement

We used PoreMatMod.jl[6] to refine the MOF structure. The organic linkers with partial occupancies in the crystal structure were replaced with linkers having no partial occupancies. Additionally, nodes from the experiment that had incorrect proton topology were substituted with nodes featuring aqua-hydroxyl ligand pairs and the correct proton topology as recommended by Planas et al.[7] After the modification, energy minimization was performed to relax both the atomic positions and cell parameters using Materials Studio version 5.0 using the Forcite module.

Density Functional Theory (DFT) calculations

Cluster DFT calculations were performed to model the interactions between a CO_2 molecule and the MOF clusters, as well as the details of the steric tuning effect of amide groups and the conformational dynamics. These calculations were performed on individual molecules, i.e. gas-phase calculations. The DFT calculations were performed using Gaussian 16, rev C.01.[8] using the M06-L functional[9] with D3 correction without damping[10]. The basis set was def2-TZVP[11, 12] on all atoms, and the def2 effective core potential (ECP) was used on Zr atoms. Interaction energies of adsorbed CO_2 molecules were corrected for basis set superposition error (BSSE) using the counterpoise correction method of Boys and Bernardi as implemented in Gaussian 16.[13] Analytical frequencies were obtained to confirm that the optimized structures are local minima on the potential energy surface and to calculate the enthalpy of adsorption at 1 atm and 298 K. Low vibrational frequency modes (< 50 cm^{-1}) were replaced with 50 cm^{-1}.[14-16]

Periodic DFT calculations were performed to calculate the dispersion interaction between a CO_2 molecule and the framework atoms. The DFT was performed using the Vienna *ab initio* Simulation Package (VASP)[17]. We used the generalized gradient approximation (GGA) exchange correlation functional from Perdew, Burke, and Ernzerhof (PBE).[18] The D3(BJ) dispersion correction was applied.[10] We employed a 400 eV plane-wave kinetic energy cutoff and a k-point mesh of 1 x 1 x 1. The convergence criterion for the self-consistent field (SCF) cycle was 10^{-6} eV.

Classical energy minimization

We performed an energy minimization using the RASPA2 software[19] to determine the lowest energy configuration of a CO_2 molecule inside the MOF. Initially, 100 random configurations of the CO_2 molecule were generated, and their positions were equilibrated with 500 NVT Monte Carlo cycles (for each initial configuration). Next, the Baker minimization algorithm,[20] as implemented in RASPA2,[19] was applied to each of the 100 equilibrated configurations. During the minimization, the framework atoms were kept rigid. The interaction energies between non-bonded atoms were calculated using the Lennard-Jones (LJ) potential using a 12.8 Å cutoff without tail correction. LJ parameters between different atom types were computed using the Lorentz-Berthelot mixing rules. Coulombic interactions were calculated using the Ewald summation technique. The LJ parameters for the framework atoms were obtained from the universal force field (UFF).[21] The partial charges for framework atoms were obtained from the DDEC6 method.[22, 23] The TraPPE force field was used to model CO_2.[24]

Grand Canonical Monte Carlo (GCMC) simulations

GCMC simulations were carried out to calculate the N_2 adsorption isotherms using the RASPA2 software.[19] The simulations consisted of 10,000 initialization cycles and 10,000 production cycles. We used translation, rotation, insertion, deletion and random reinsertion Monte Carlo moves. The interaction energies between non-bonded atoms were calculated using the Lennard-Jones (LJ) potential using a 12.8 Å cutoff without tail correction. LJ parameters between different atom types

were computed using the Lorentz-Berthelot mixing rules. The framework atoms were kept rigid during the simulations. Coulombic interactions were calculated using the Ewald summation technique. The LJ parameters for the framework atoms were obtained from the universal force field (UFF).[21] The partial charges for framework atoms were obtained from the DDEC6 method.[22, 23] The TraPPE force field was used to model N_2.[24]

Pore structure compartmentalization

We used Zeo++ to compute the pore size distribution (PSD) of the MOF with N_2 as the probe molecule.[25] To clearly visualize the inherent channels of the MOF, we then implemented an algorithm called pyCOSMOS,[26] which partitions the MOF structure into distinct pore compartments. The generated PSD file (vpsdpts file) and the optimized cif file were used as the input file for the code. The parameters of the DBSCAN algorithm were set as default (eps=2.500 and nmin=25). The code then identified three pore types for the MOF. The different pore types were further filled with small spheres with different colors and visualized using CrystalMaker 11.1.

Isosteric heats of adsorption (Q_{st})

Three experimental CO_2 single-component isotherms ($\Delta T \leq 20\ K$) at 278 K, 288 K, 298 K were fitted with the virial equation:[27]

$$\ln(P) = \ln n + \frac{1}{T}\sum_{i=0}^{m} a_i n^i + \sum_{i=0}^{n} b_i n^i \qquad (1)$$

where P is pressure (kPa), n is the amount of adsorbed CO_2 (mmol g^{-1}), T is the temperature (K), a_i and b_i are virial coefficients, and m and n are the number of coefficients required to fit the isotherms. Then, the Q_{st} values for CO_2 were calculated based on the fitting parameters using the equation,

$$Q_{St} = -R\sum_{i=0}^{m} a_i n^i \qquad (2)$$

where R is the universal gas constant (8.314 J K^{-1} mol^{-1}).

Ideal adsorbed solution theory (IAST) selectivity

The experimentally collected isotherms for CO_2, CH_4, and N_2 at 298 K were fitted with the single-site Langmuir-Freundlich equation,

$$n = q_s \frac{bp^v}{1 + bp^v} \qquad (3)$$

where n is the uptake of adsorbate per mass of adsorbent (mmol g^{-1}), q_s is the saturation capacity (mmol g^{-1}), b is the affinity coefficient (kPa^{-1}), p is the pressure of the bulk gas at equilibrium with the adsorbate phase, and v is the Freundlich constant. Then, the selectivity was calculated based on IAST[28] using the normal definition of selectivity:

$$S_{ads} = \frac{q_1/q_2}{y_1/y_2} \qquad (4)$$

where q_1 and q_2 represent the molar loading of each component (mmol g^{-1}), within the MOF that is in equilibrium with a bulk fluid mixture with mole fractions y_1, and y_2=1-y_1. In the IAST selectivity calculation of CO_2/CH_4 (v/v=10:90) mixture, the calculations were performed for mole fractions y_1=0.1 and y_2=0.9 for a range of pressures up to 1 bar and 298 K.

S4. Synthesis

Synthesis of monomer

Synthesis of hexamethyl 4,4',4'',4''',4'''',4'''''-(benzene-1,3,5-triyltris(3,5-dicyanopyridine-4,2,6-triyl))hexabenzoate (Me_6CN-BTP): Methyl 4-(cyanoacetyl)benzoate (7.2 mmol, 1.463 g), benzene-1,3,5-tricarboxaldehyde (1 mmol, 0.162 g), and ammonium acetate (15 mmol, 1.156 g) were discharged into the reaction flask, then 30 ml acetic acid was added. The reaction mixture was heated to reflux overnight. After adding water, the resultant precipitates were filtered and washed with water. Then, the solids were oxidized with sodium nitrite (1.035 g, 15 mmol) added in portions in acetic acid solution (30 ml) at room temperature for 1h and then 80 ºC for 1 h. After cooling, the suspension was poured onto ice water, and the precipitates were filtered and washed with water. The crude product was purified by recrystallization from ethyl acetate/methanol solution and washed with methanol to yield product Me_6CN-BTP as a white to yellow solid (around 0.78 g, yield: 61.7%). ^{1}H NMR (500 MHz, DMSO) δ 8.76 (3H), 8.21 (24H), 3.92 (18H). ^{13}C NMR (126 MHz, DMSO) δ 166.10, 162.41, 157.20, 140.76, 135.63, 132.95, 132.35, 130.46, 129.93, 115.43, 107.92, 52.99. Chemical Formula: $C_{75}H_{45}N_9O_{12}$. HRMS (ESI, m/z): $[M+Na]^+$ calculated 1286.30799; found 1286.30833.

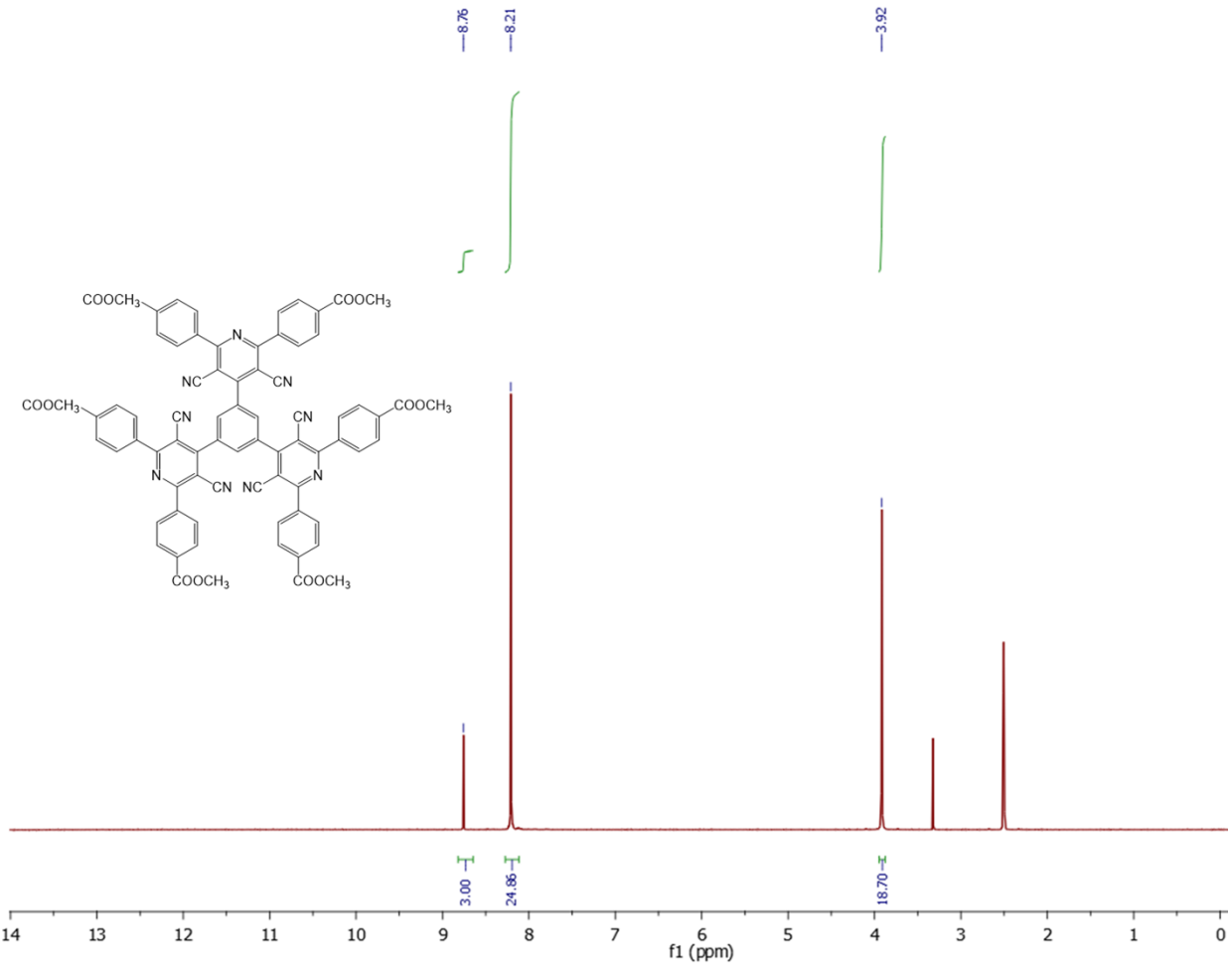

Figure S1. ^{1}H NMR spectrum of the Me_6CN-BTP molecule in DMSO-d_6.

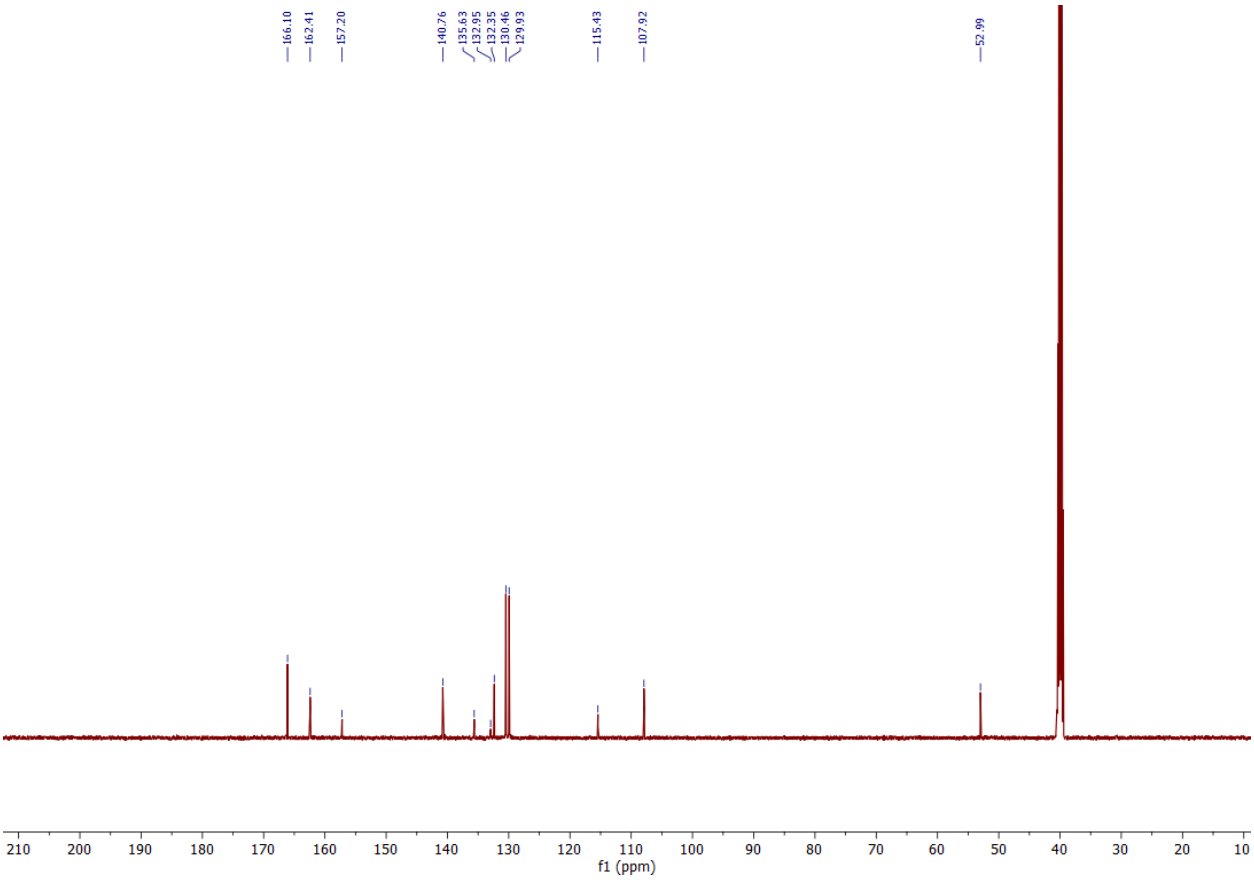

Figure S2. ^{13}C NMR spectrum of the Me_6CN-BTP molecule in DMSO-d_6.

Synthesis of 4,4',4'',4''',4'''',4'''''-(benzene-1,3,5-triyltris(3,5-dicarbamoylpyridine-4,2,6-triyl))hexabenzoic acid (H_6AM-BTP): Me_6CN-BTP (0.17 mmol, 0.220 g) was suspended in 10 mL mixture of methanol and THF with volume ratio of 1:1. After adding 5 mL of KOH aqueous solution (4.3M), the solution was heated to reflux for 36 hours. After cooling down to room temperature, THF and methanol were removed under reduced pressure. The resulting aqueous solution was filtered and acidified to pH 3−5 with diluted aqueous HCl (6M), and the precipitate was separated by filtration, washed successively with water, and dried under vacuum, to yield product of H_6AM-BTP as a white to yellow solid (around 0.202 g, yield: 91.8%). ^1H NMR (500 MHz, DMSO) δ 13.07 (6H), 8.06−7.90 (24H), 7.57 (3H), 7.36 (6H), 7.02 (6H). ^{13}C NMR (126 MHz, DMSO) δ 168.38, 167.56, 153.56, 145.49, 143.68, 134.35, 131.94, 131.57, 129.95, 129.53, 129.37. Chemical Formula: $C_{69}H_{45}N_9O_{18}$. HRMS (ESI, m/z): $[M+H]^+$ calculated 1288.29553; found 1288.29505.

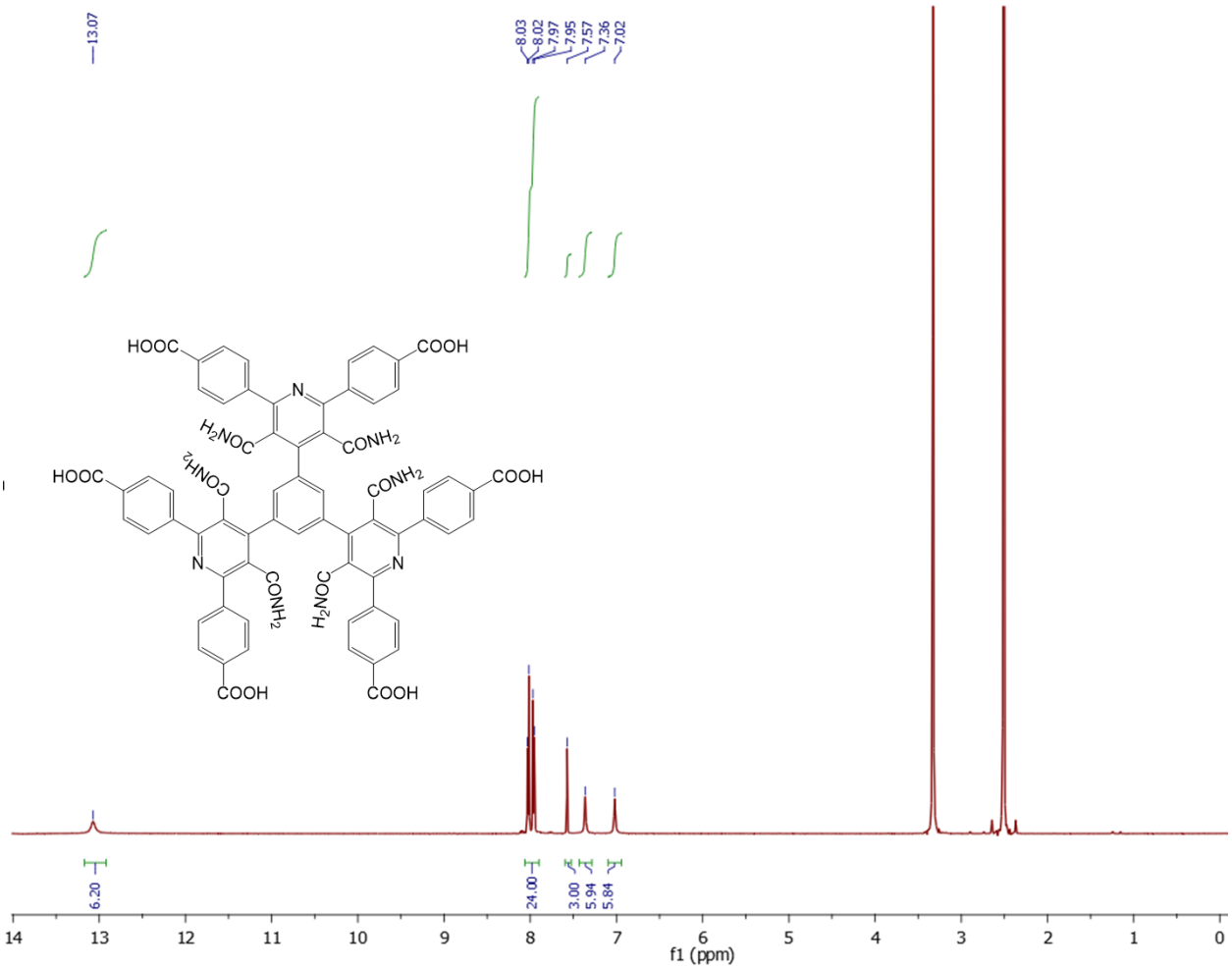

Figure S3. ^{1}H NMR spectrum of the H_6AM-BTP molecule in DMSO-d_6.

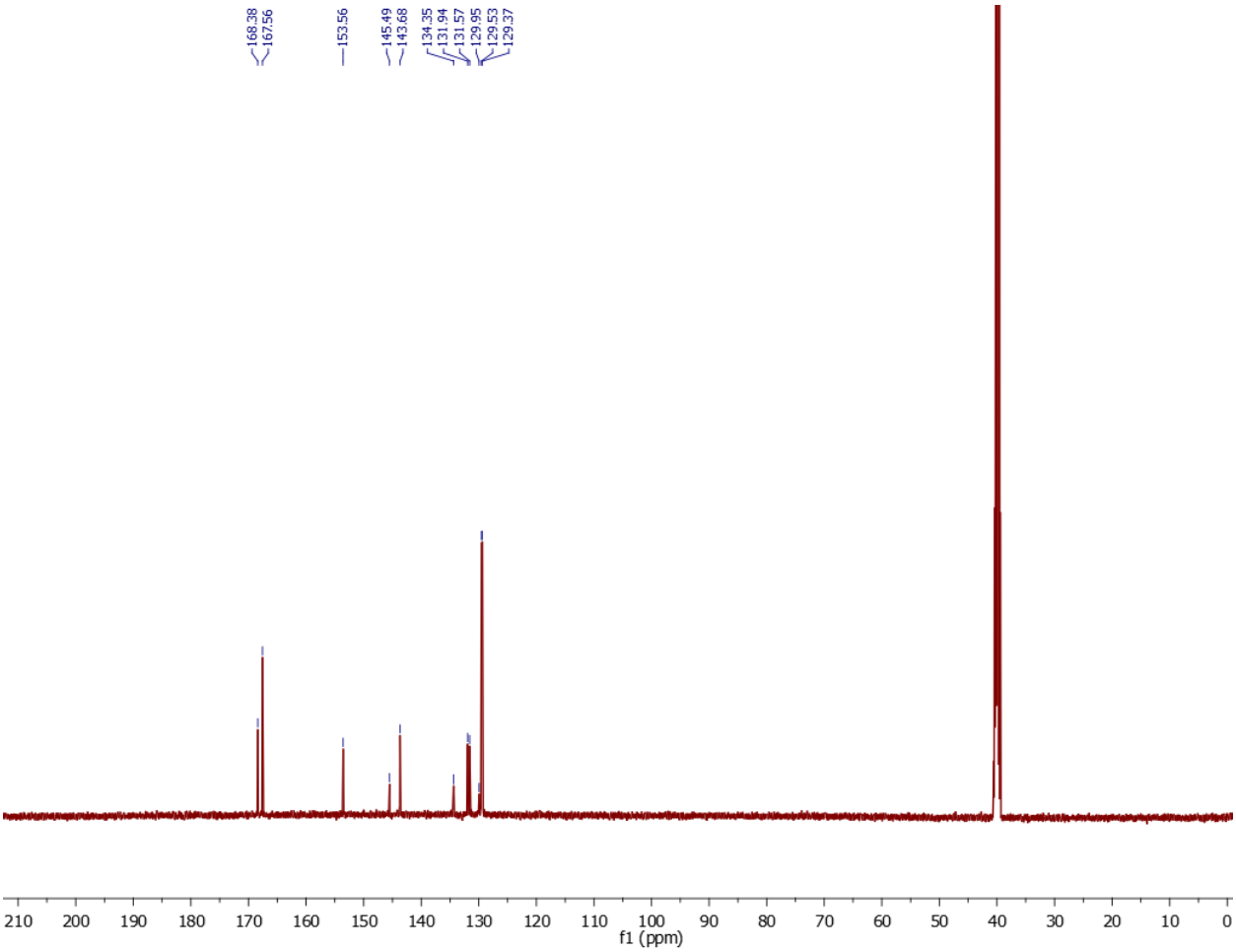

Figure S4. ^{13}C NMR spectrum of the H_6AM-BTP molecule in DMSO-d_6.

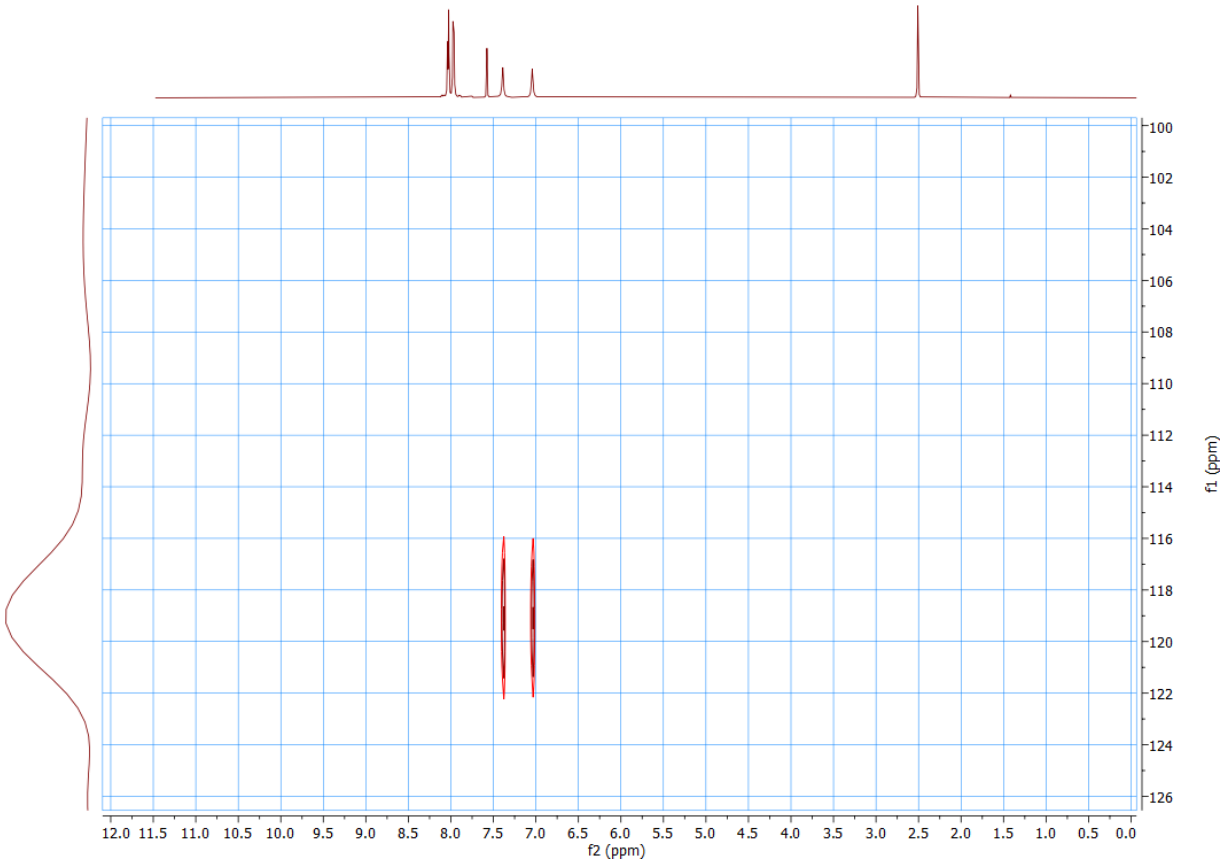

Figure S5. $^{1}H-^{15}N$ HSQC spectrum (vertical, ^{15}N; horizontal, ^{1}H) of the H_6AM-BTP molecule in DMSO-d_6.

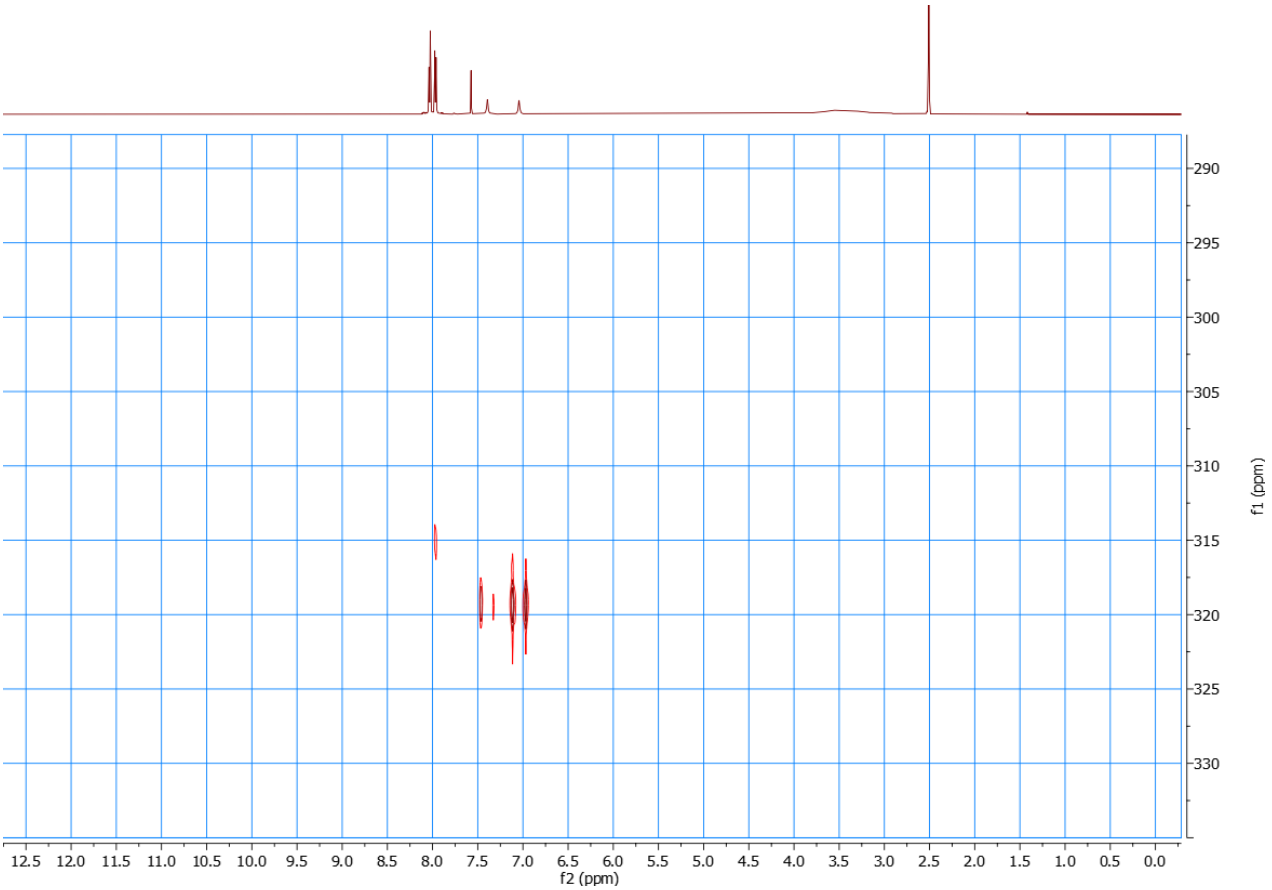

Figure S6. $^{1}H-^{15}N$ HMBC spectrum (vertical, ^{15}N; horizontal, ^{1}H) of the H_6AM-BTP molecule in DMSO-d_6. Four bond correlations of N (pyridine) and H (carboxylate phenyl ring).

Synthesis of 4,4',4'',4''',4'''',4'''''-(benzene-1,3,5-triyltris(3,5-dicyanopyridine-4,2,6-triyl))hexabenzoic acid (H_6CN-BTP): 4-(2-Cyanoacetyl)benzoic acid (3.6 mmol, 0.681 g), benzene-1,3,5-tricarboxaldehyde (0.5 mmol, 0.081 g), and ammonium acetate (7.5 mmol, 0.578 g) were discharged into the reaction flask, then 20 ml acetic acid was added. The reaction mixture was heated to reflux overnight. After adding water, the resultant precipitates were filtered and washed with water. Then, the solids were oxidized with sodium nitrite (1.035 g, 15 mmol) added in portions in acetic acid solution (20 ml) at room temperature for 1h and then 100 ºC for 1 h. After cooling, the suspension was poured onto ice water, and the precipitates were filtered. The crude product was then washed with diluted ammonium hydroxide solution, filtered, and acidified to pH 3−5 with diluted aqueous HCl (6M). The precipitate was separated by filtration, washed successively with water, recrystallized from acetic acid and hexane, and dried under vacuum, yielding product H_6CN-BTP as a white to yellow solid (around 0.24 g, yield: 40.7%). ^{1}H NMR (500 MHz, DMSO) δ 8.76 (3H), 8.18 (24H). ^{13}C NMR (126 MHz, DMSO) δ 167.15, 162.54, 157.24, 140.40, 135.64, 133.64, 132.97, 130.32, 130.04, 115.50, 107.76. Chemical Formula: $C_{63}H_{33}N_9O_{12}$. HRMS (ESI, m/z): $[M+Na]^+$ calculated 1202.21409; found 1202.21371.

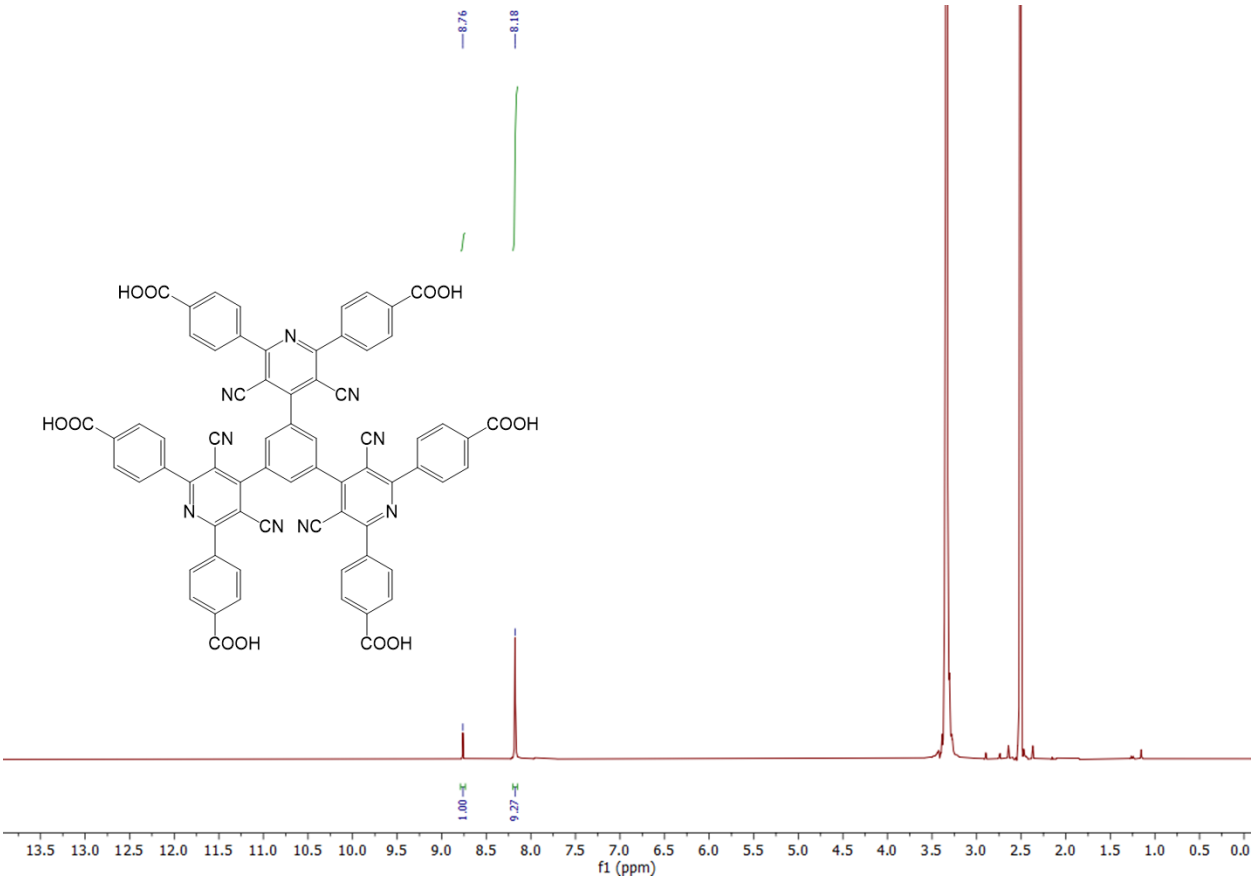

Figure S7. ^{1}H NMR spectrum of the H_6CN-BTP molecule in DMSO-d_6.

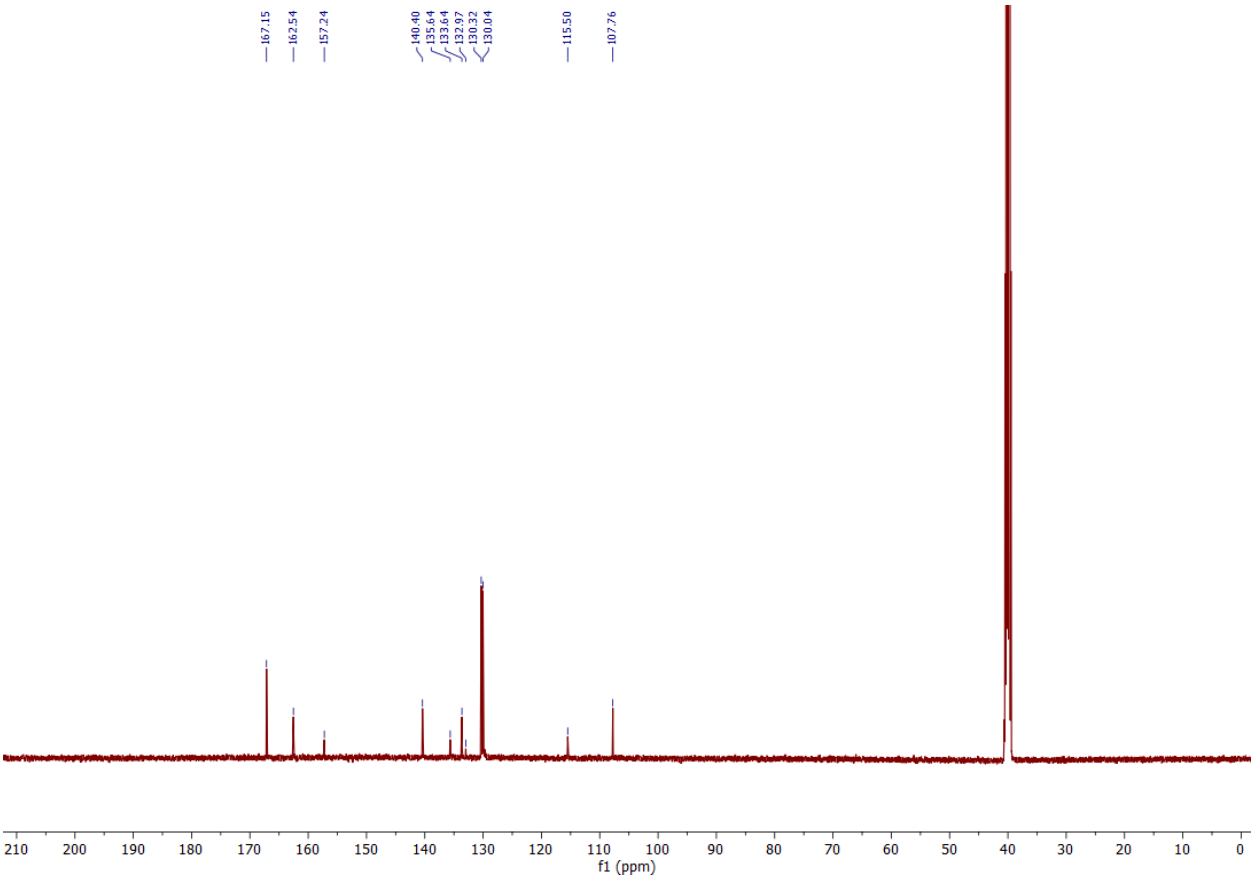

Figure S8. ^{13}C NMR spectrum of the H_6CN-BTP molecule in DMSO-d_6.

Synthesis of 4,4',4'',4'''-(benzene-1,3-diylbis(3,5-dicyanopyridine-4,2,6-triyl)) tetrabenzoic acid (H_4CN-MBBP): 4-(2-Cyanoacetyl)benzoic acid (0.6 mmol, 0.113 g), 2,5-dimethoxybenzene-1,4-dicarboxaldehyde (0.1 mmol, 0.019 g), and ammonium acetate (2 mmol, 0.154 g) were discharged into the reaction flask, then 4 ml acetic acid was added. The reaction mixture was heated to reflux overnight. After adding water, the resultant precipitates were filtered and washed with water. Then, the solids were oxidized with sodium nitrite (0.207 g, 3 mmol) added in portions in acetic acid solution (4 ml) at 95 ºC for 1 h. After cooling, the suspension was poured onto ice water, and the precipitates were filtered. The crude product was then washed with diluted ammonium hydroxide solution, filtered, and acidified to pH 3−5 with diluted aqueous HCl (6M). The precipitate was separated by filtration, washed successively with water and dried under vacuum, yielding product H_4CN-MBBP as a yellow brown solid (around 0.051 g, yield: 58.4%). ^1H NMR (500 MHz, DMSO) δ 8.20 (16H), 7.78 (2H). ^{13}C NMR (126 MHz, DMSO) δ 167.16, 162.14, 156.36, 150.38, 140.43, 133.50, 130.29, 130.03, 125.71, 115.81, 115.61, 108.56, 57.17.

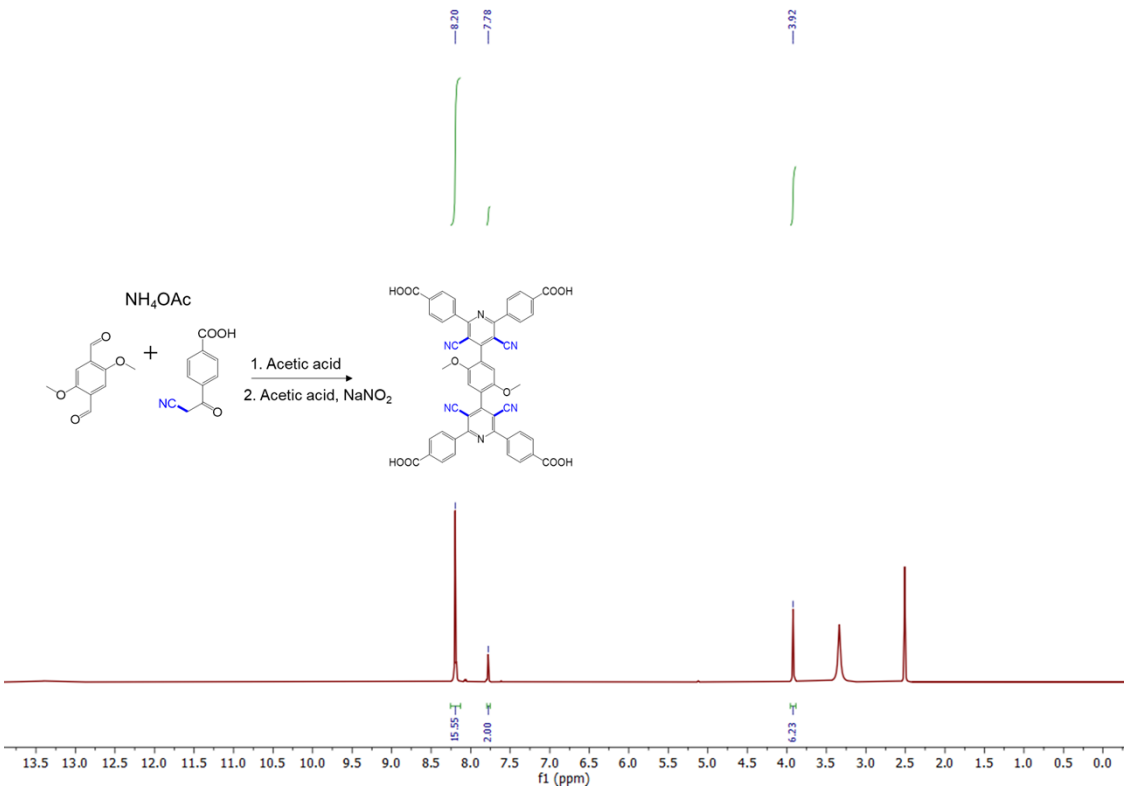

Figure S9. ^{1}H NMR spectrum of the H_4CN-MBBP molecule in DMSO-d_6.

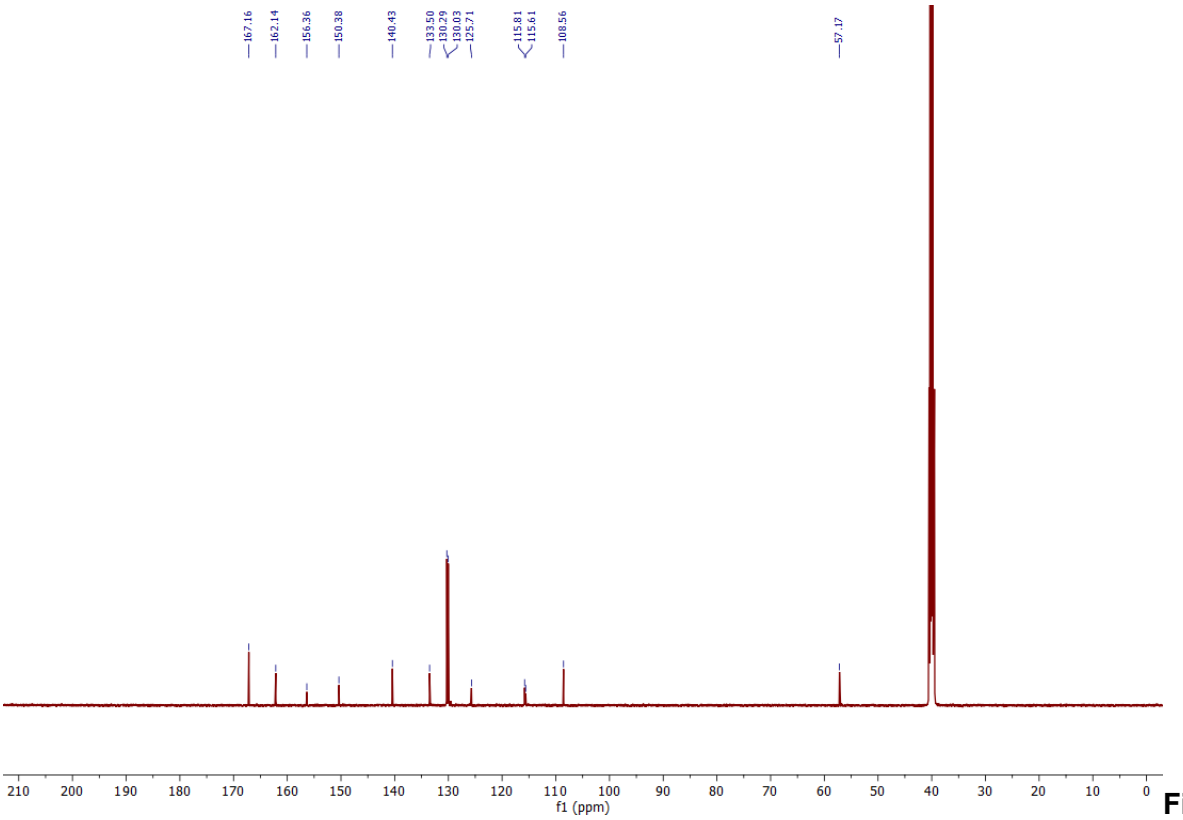

Figure S10. ^{13}C NMR spectrum of the H_4CN-MBBP molecule in DMSO-d_6.

Synthesis of 4,4',4'',4''',4'''',4'''''-(benzene-1,3,5-triyltris(3,5-dicyanopyridine-4,2,6-triyl))hexabenzoic acid (H_4CN-BMBP): 4-(2-Cyanoacetyl)benzoic acid (0.6 mmol, 0.113 g), isophthalaldehyde (0.1 mmol, 0.013 g), and ammonium acetate (2 mmol, 0.154 g) were discharged into the reaction flask, then 4 ml acetic acid was added. The reaction mixture was heated to reflux overnight. After adding water, the resultant precipitates were filtered and washed with water. Then, the solids were oxidized with sodium nitrite (0.207 g, 3 mmol) added in portions in acetic acid solution (4 ml) at 95 ºC for 1 h. After cooling, the suspension was poured onto ice water, and the precipitates were washed with water and acetone. The acetone solution was dried to give crude product, which was then washed with diluted ammonium hydroxide solution, filtered, and acidified to pH 3−5 with diluted aqueous HCl (6M). The precipitate was separated by filtration, washed successively with water and dried under vacuum, yielding product H_4CN-BMBP as a write yellow solid (around 0.026 g, yield: 31.4%). ^{1}H NMR (500 MHz, DMSO) δ 8.36 (1H), 8.16 (16H), 8.18−8.15 (2H), 8.05−8.00 (1H). ^{13}C NMR (126 MHz, DMSO) δ 167.16, 162.30, 158.58, 140.48, 134.90, 133.51, 132.09, 130.30, 130.01, 129.74, 129.09, 115.87, 107.84.

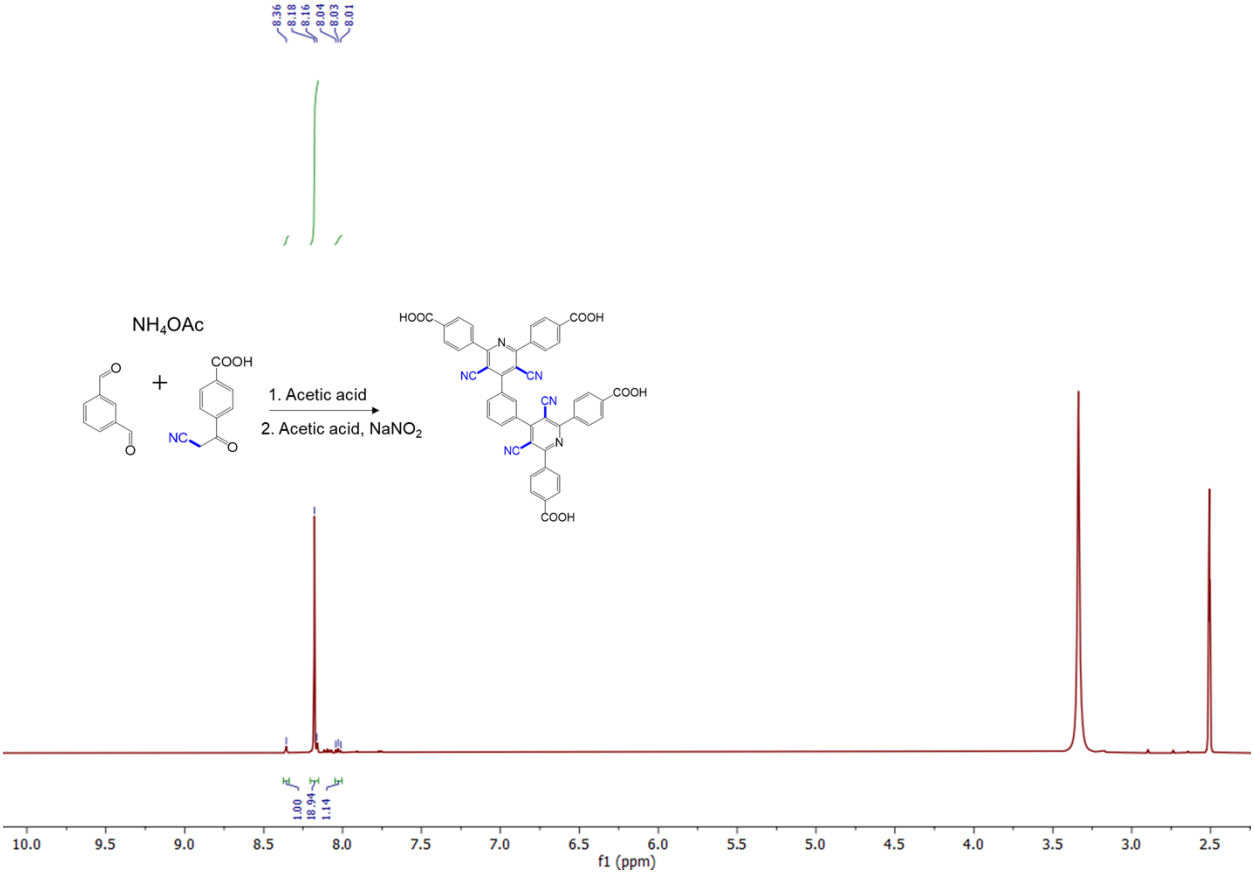

Figure S11. ^{1}H NMR spectrum of the H_4CN-BMBP molecule in DMSO-d_6.

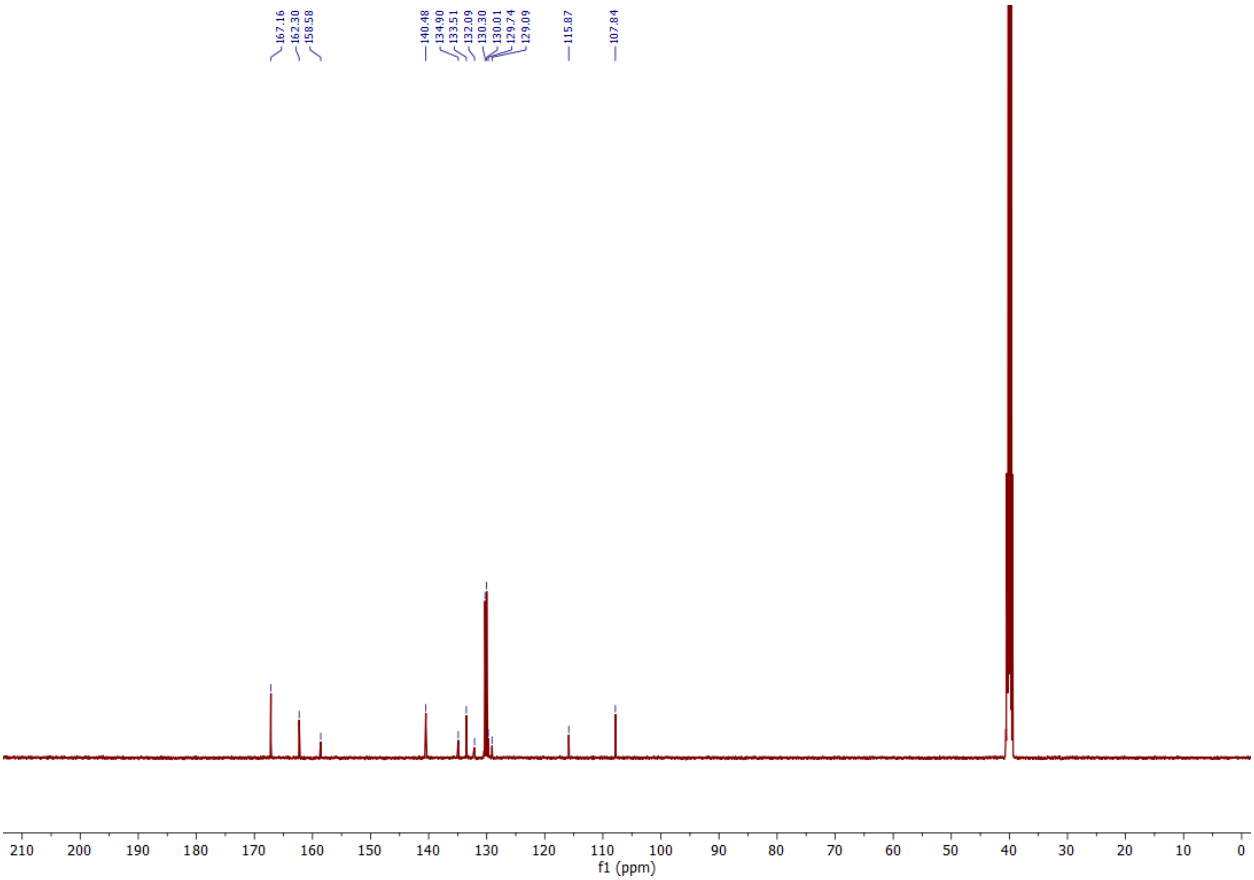

Figure S12. ^{13}C NMR spectrum of the H_4CN-BMBP molecule in DMSO-d_6.

Synthesis of 4,4',4'',4''',4'''',4'''''-(benzene-1,3,5-triyltris(3,5-dicyanopyridine-4,2,6-triyl))hexakis(4-bromophenyl) (Br_6CN-BTP): (4-bromobenzoyl)acetonitrile (0.72 mmol, 0.161 g), 2,5-benzene-1,3,5-tricarboxaldehyde (0.1 mmol, 0.016 g), and ammonium acetate (3 mmol, 0.231 g) were discharged into the reaction flask, then 4 ml acetic acid was added. The reaction mixture was heated to reflux overnight. After adding water, the resultant precipitates were filtered and washed with water and acetone. The solids were dried, then oxidized with sodium nitrite (0.311 g, 4.5 mmol) added in portions in acetic acid solution (4 ml) at 95 ºC for 1 h. After cooling, the suspension was poured onto ice water, and the precipitates were filtered. The product was then separated by filtration, washed successively with water and dried under vacuum, yielding product (Br_6CN-BTP) as a write to yellow solid (around 0.101 g, yield: 73.0%). ^1H NMR (500 MHz, DMSO) δ 8.70 (3H), 8.05−7.85 (24H). ^{13}C NMR (126 MHz, DMSO) δ 162.20, 157.30, 135.78, 135.62, 132.93, 132.35, 132.01, 125.98, 115.62, 107.03.

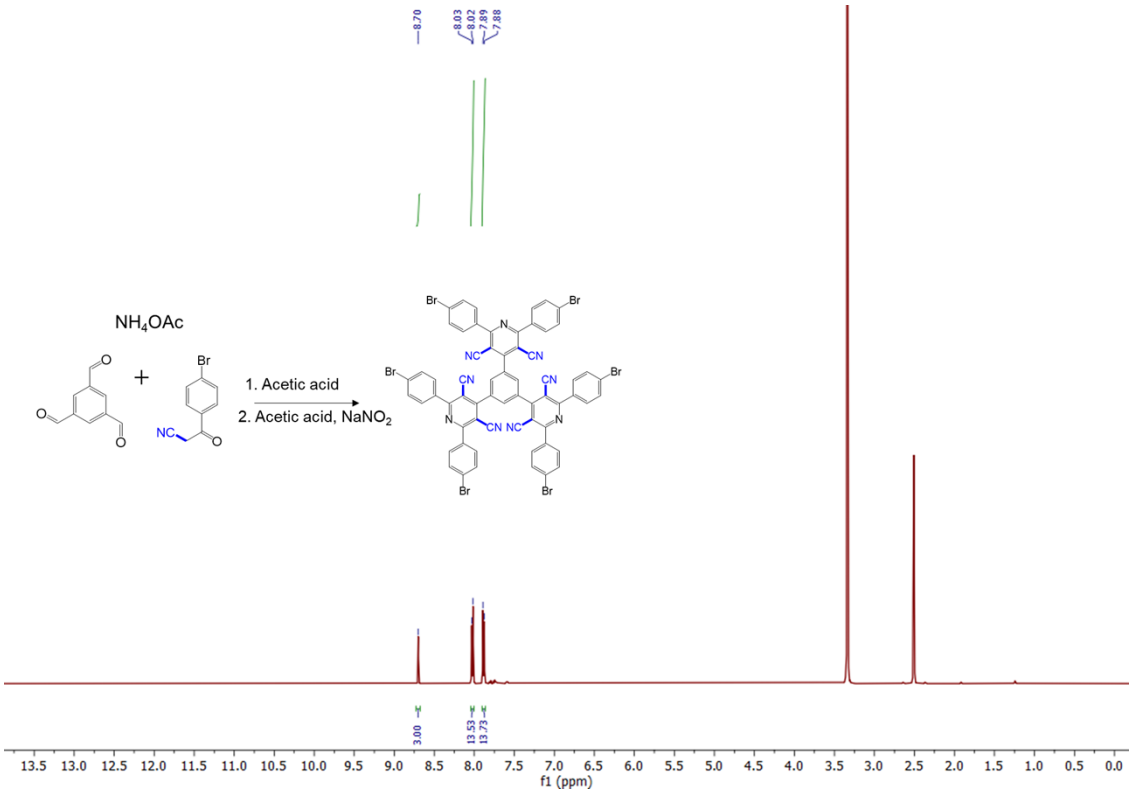

Figure S13. ^{1}H NMR spectrum of the Br_6CN-BTP molecule in DMSO-d_6.

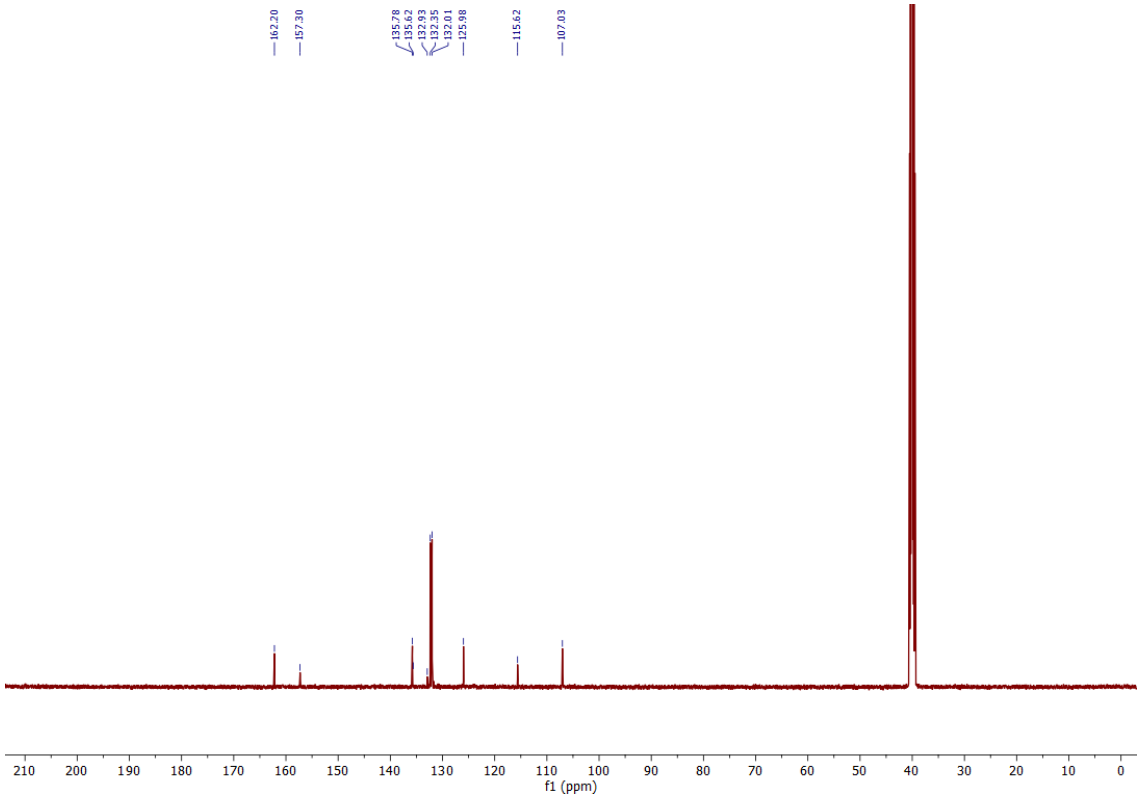

Figure S14. ^{13}C NMR spectrum of the Br_6CN-BTP molecule in DMSO-d_6.

Synthesis of AM-Zr-1 crystal: $ZrCl_4$ (0.6 mg in 0.2 mL DEF from stock solutions, 0.0026 mmol) and H_6AM-BTP (0.8 mg in 0.2 mL DEF from stock solutions, 0.0006 mmol) were mixed and sealed in a 3 mL glass vial. Then, 0.16 mL of formic acid was added to the mixture, followed by sonication for 5 min. The resultant mixture was heated to 120 °C for 3 days. Colorless plate crystals were obtained and used for single-crystal X-ray diffraction measurements.

Synthesis of AM-Zr-1 micro-crystalline powder: $ZrCl_4$ (29.5 mg in 5 mL DMF, 0.127 mmol) and H_6AM-BTP (36.0 mg in 5 mL DMF, 0.028 mmol) were mixed and sonicated for 2 min. After adding 4 mL of formic acid, the mixture was sonicated for 2 min. This solution was then divided between two 20 mL glass vials and heated to 120 °C for 3 days. The microcrystalline white powder was obtained through centrifugation, washed with DMF three times, and soaked in DMF overnight. The material was then washed with acetone six times over two days. After soaking in acetone overnight, the material was activated by supercritical CO_2 drying, giving activated AM-Zr-1 MOF (yield: ~31 mg) for gas sorption measurements.

Synthesis of CN-Zr-1 crystal: $ZrCl_4$ (0.8 mg in 0.2 mL DMF from stock solutions, 0.0035 mmol) and H_6CN-BTP (0.8 mg in 0.2 mL DMF from stock solutions, 0.0007 mmol) were mixed and sealed in a 3 mL glass vial. Then, 100 mg of benzoic acid was added to the mixture, followed by sonication for 5 min. The resultant mixture was heated to 120 °C for 3 days. Colorless plate crystals were obtained and used for single-crystal X-ray diffraction measurements.

Synthesis of CN-Zr-1 micro-crystalline powder: $ZrCl_4$ (22.0 mg in 3 mL DMF, 0.095 mmol) and H_6CN-BTP (24.7 mg in 3 mL DMF, 0.021 mmol) were mixed and sonicated for 2 min. After adding 1.2 mL of formic acid, the mixture was sonicated for 2 min. This solution was then divided between two 20 mL glass vials and heated to 120 °C for 3 days. The microcrystalline white powder was obtained through centrifugation, washed with DMF three times, and soaked in DMF overnight. The material was then washed with acetone six times over two days. After soaking in acetone overnight, the material was activated by supercritical CO_2 drying, giving activated CN-Zr-1 MOF (yield: ~26 mg) for gas sorption measurements.

S5. Additional Figures and Tables

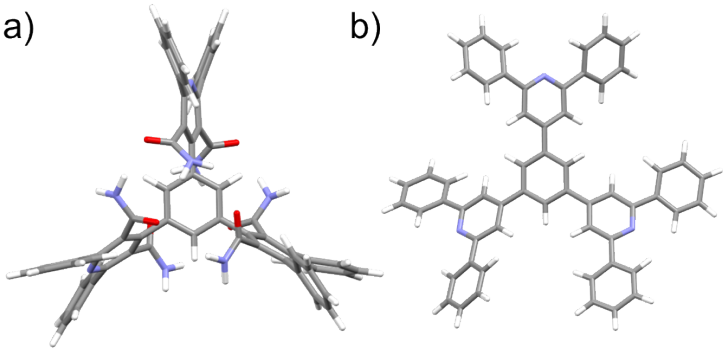

Figure S15. Lowest-energy molecular conformations of (a) H_6AM-BTP and (b) a control molecule without steric tuning on side arms, as determined by relaxed energy scan performed at the M06-L+D3/Def2-TZVP level of theory. The COOH groups in these molecules were replaced by H atoms to reduce the computational cost.

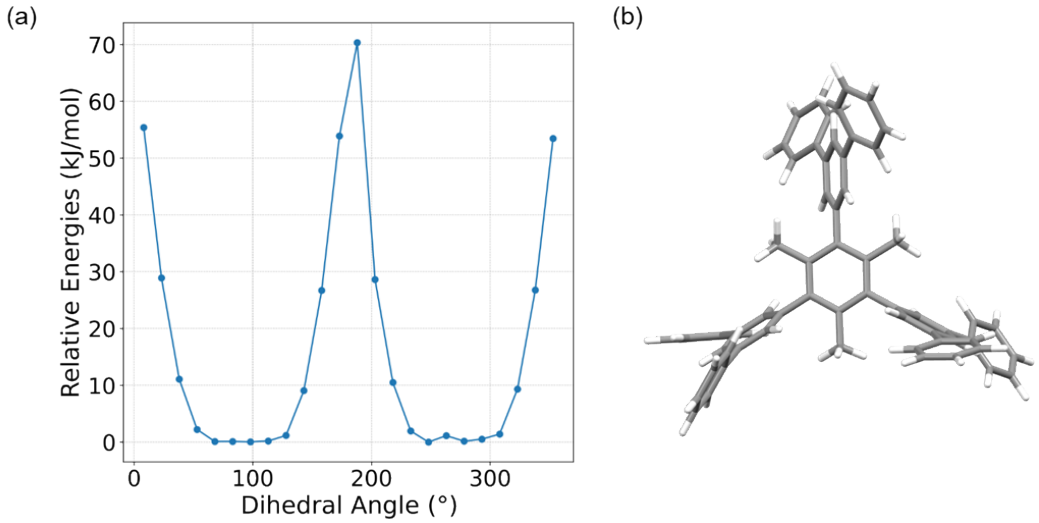

Figure S16. (a) Relaxed energy scan of a simplified model of the published molecule (Me-TDCPB)[29] performed at the M06-L+D3/Def2-TZVP level of theory. The COOH groups in this molecule were replaced by H atoms to reduce the computational cost. (b) Molecular conformation with the lowest energy. The dihedral angle is defined between the central phenyl and its connected phenyl ring and scanned every 15°.

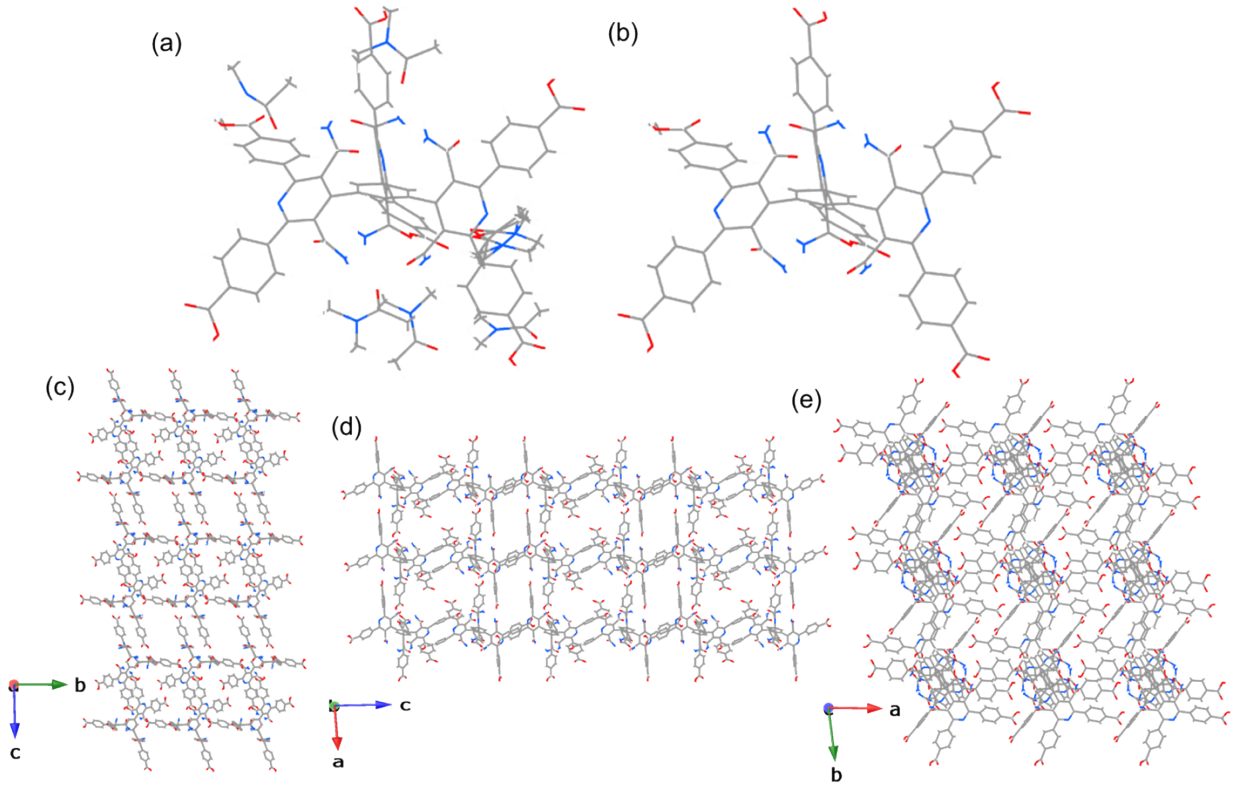

Figure S17. Single crystal structure of the crystal C1 grown by diffusion of ethyl ether to DMAC (C, grey; N, blue; O, red; H, white). Solvents are omitted in (b–e).

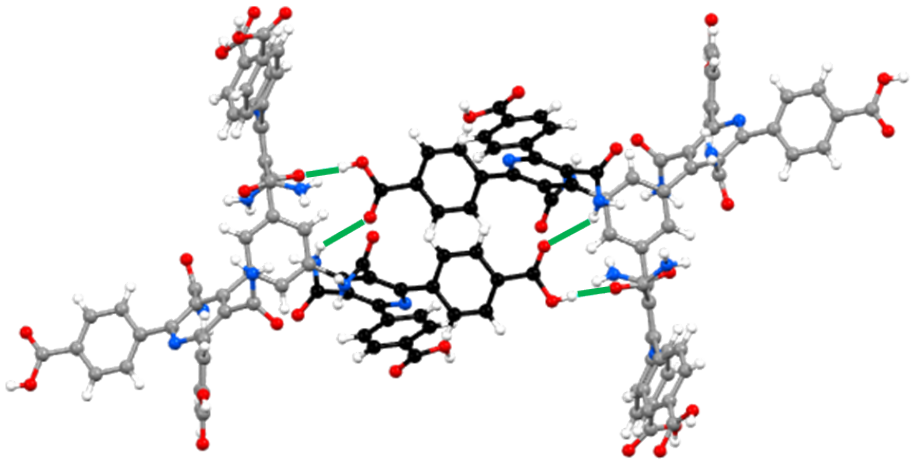

Figure S18. The “terminal-to-central" carboxylic acid···amide hydrogen bond in C1 (DCMP arm highlighted black). H_6AM-BTP uses one of its three DCMP arms (arm 1) to form intermolecular carboxylic acid···amide hydrogen bond ($O_{carboxylic\ acid}$–H···O=C_{amide} and C=$O_{carboxylic\ acid}$···H–N_{amide}). The hydrogen bond is highlighted green (C, grey and black; N, blue; O, red; H, white).

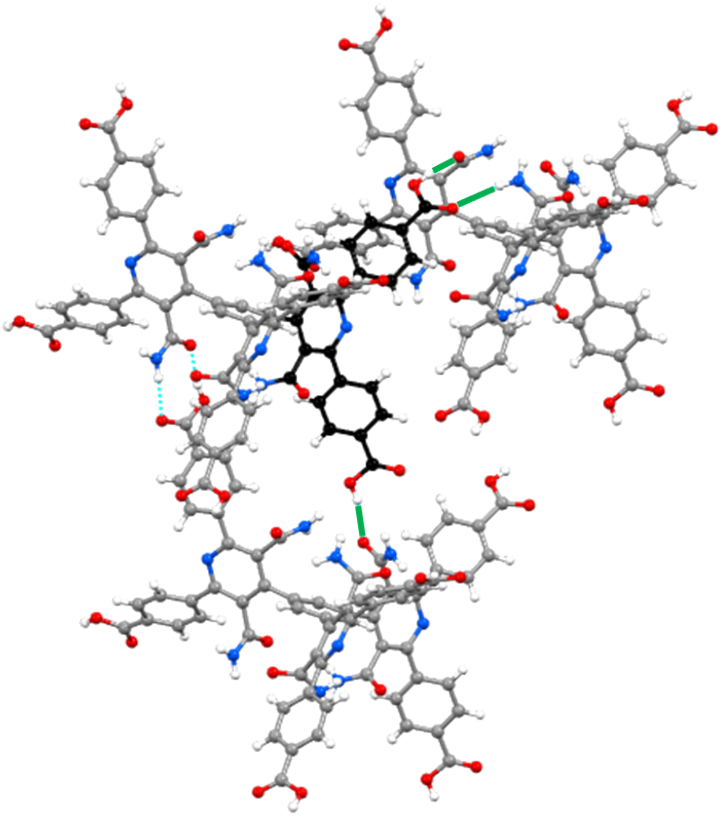

Figure S19. The “terminal-to-central" carboxylic acid···amide hydrogen bond in C1 (DCMP arm highlighted black). H_6AM-BTP uses another DCMP arms (arm 2) to form intermolecular carboxylic acid···amide hydrogen bond ($O_{carboxylic\ acid}$–H···O=C_{amide} and C=$O_{carboxylic\ acid}$···H–N_{amide}). The hydrogen bond is highlighted green (C, grey and black; N, blue; O, red; H, white).

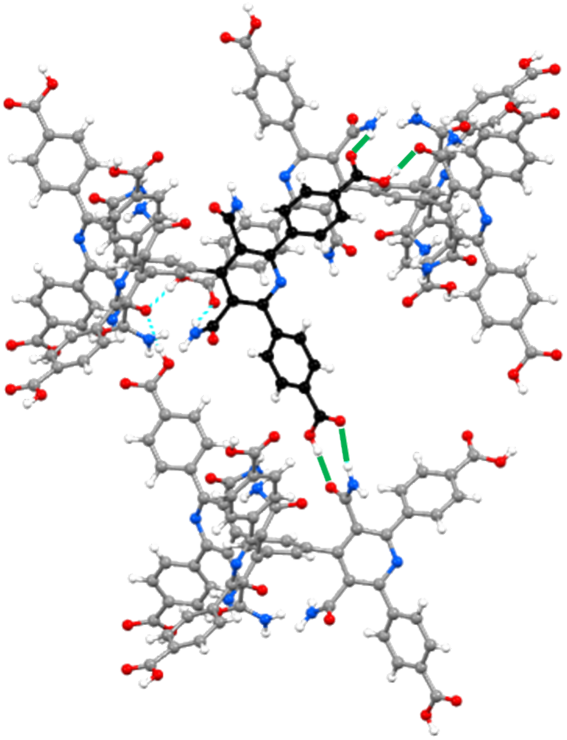

Figure S20. The “terminal-to-central" carboxylic acid···amide hydrogen bond in C1 (DCMP arm highlighted black). H_6AM-BTP uses another DCMP arms (arm 3) to form intermolecular carboxylic acid···amide hydrogen bond ($O_{carboxylic\ acid}$–H···O=C_{amide} and C=$O_{carboxylic\ acid}$···H–N_{amide}). The hydrogen bond is highlighted green (C, grey and black; N, blue; O, red; H, white). Notably, in contrast to the hydrogen bonding mode observed in the other two arms—where each amide group functions exclusively as either a hydrogen bond donor or acceptor—the amide group in this arm simultaneously acts as both a donor and an acceptor.

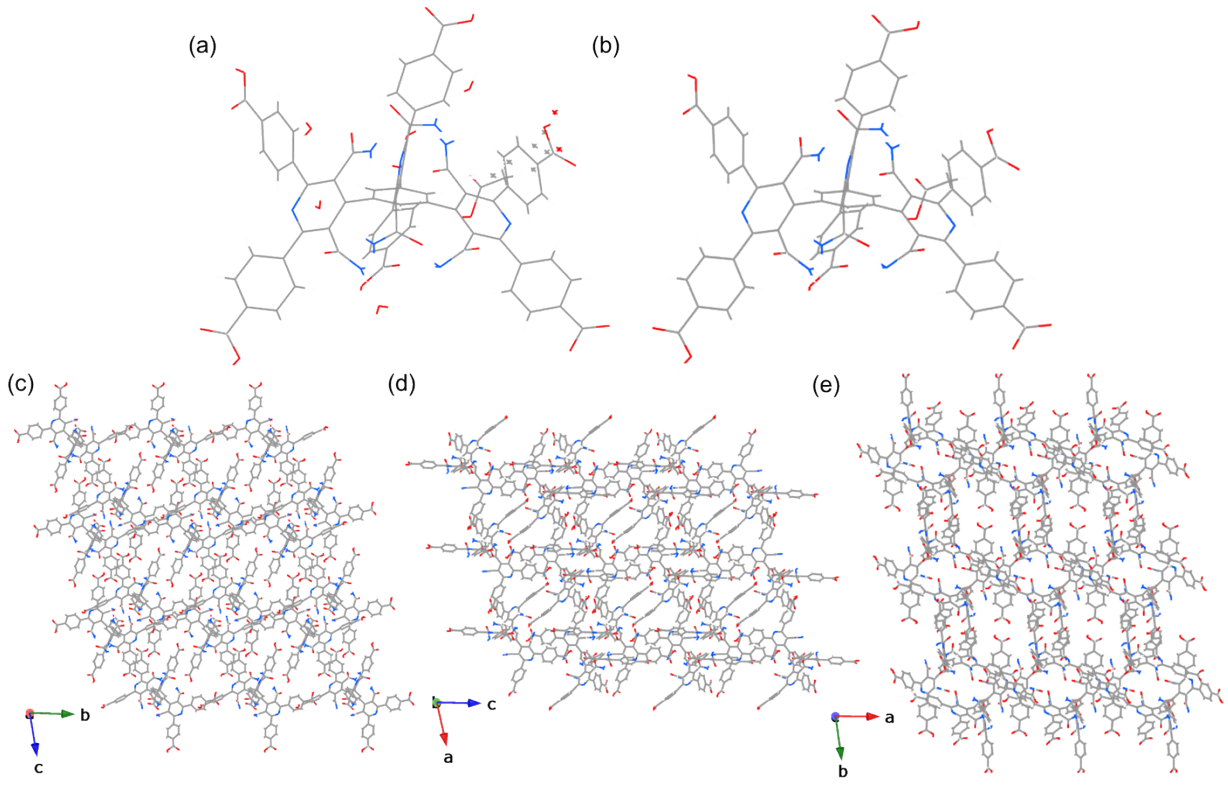

Figure S21. Single crystal structure of the crystal C2 grown by diffusion of hexane to acetic acid (C, grey; N, blue; O, red; H, white). Solvents are omitted in (b–e).

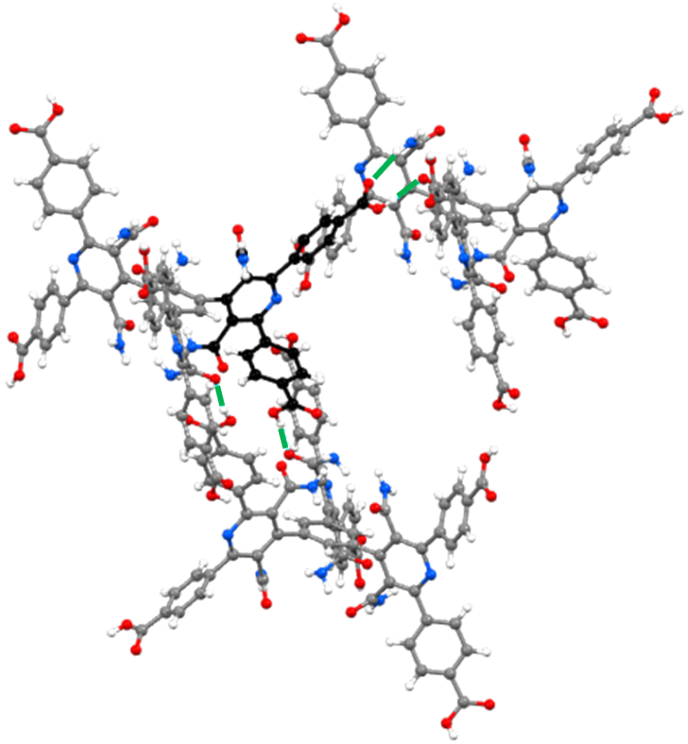

Figure S22. The “terminal-to-central" carboxylic acid···amide hydrogen bond in C2 (DCMP arm highlighted black). H_6AM-BTP uses the third DCMP arms to form intermolecular carboxylic acid···amide hydrogen bond ($O_{carboxylic\ acid}$–H···O=C_{amide} and C=$O_{carboxylic\ acid}$···H–N_{amide}). The hydrogen bond is highlighted green (C, grey and black; N, blue; O, red; H, white).

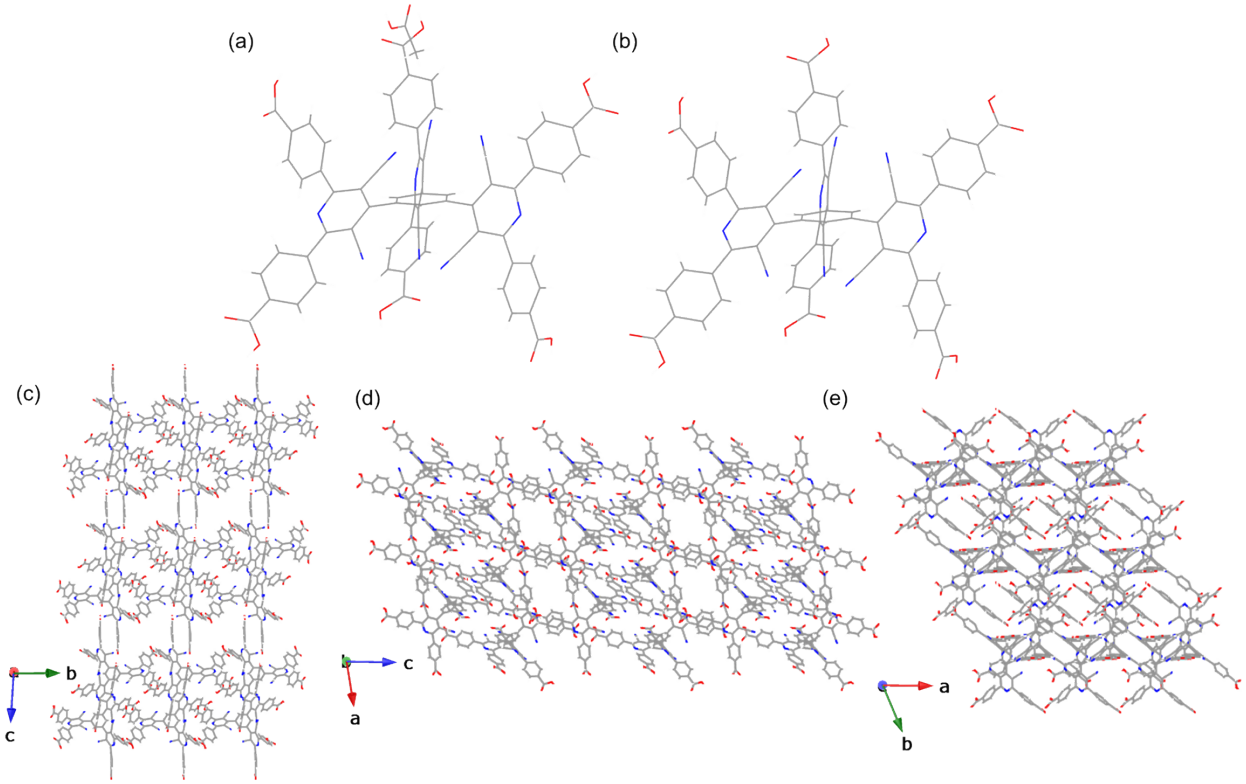

Figure S23. Single crystal structure of the crystal C3 grown by diffusion of hexane to acetic acid (C, grey; N, blue; O, red; H, white). Solvents are omitted in (b–e).

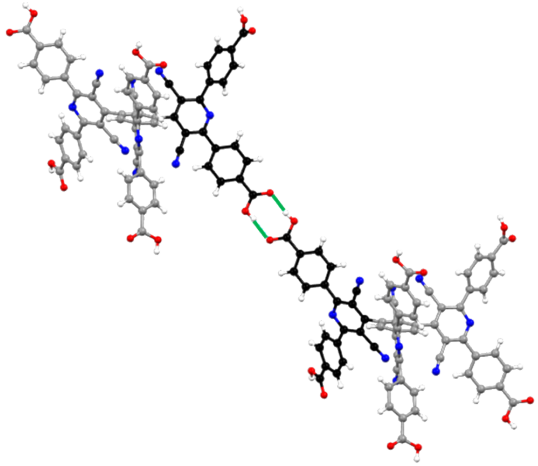

Figure S24. The “terminal-to-central" carboxylic acid···carboxylic acid hydrogen bond in C3 (DCNP arm highlighted black). The hydrogen bond is highlighted green (C, grey and black; N, blue; O, red; H, white).

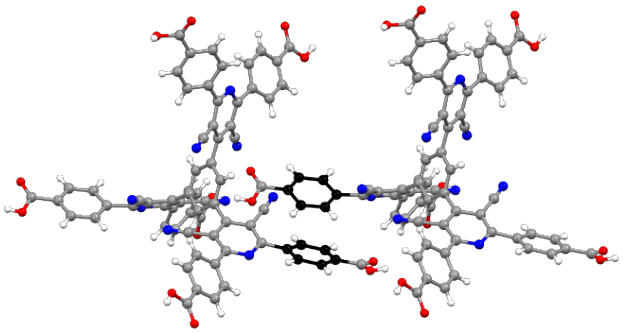

Figure S25. Benzene···Benzene π–π stacking of H_6CN-BTP in C3 (Benzene ring highlighted black). C, grey and black; N, blue; O, red; H, white.

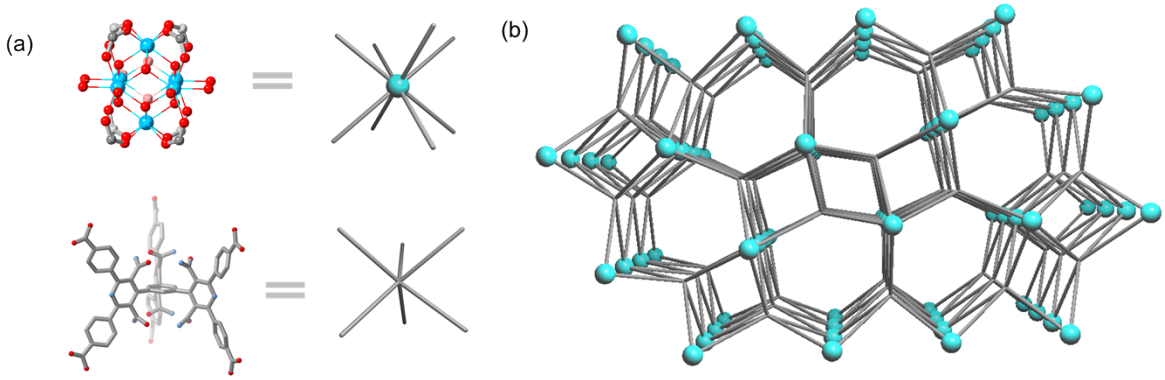

Figure S26. (a) The simplified view of the Zr_6 SBU node (8-c blue dot) and organic linker (6-c silver rod). (b) The 6,8-c *nuh*1 underlying net resulting from the single node cluster description method by using ToposPro software.

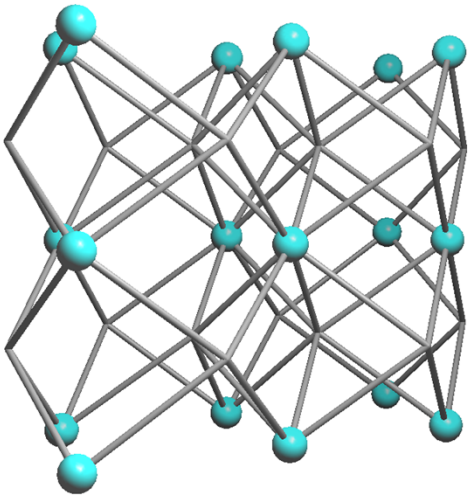

Figure S27. Simplified *nuh*1 underlying net of AM-Zr-1. Blue dot represents the Zr_6 node and silver rod represents H_6AM-BTP.

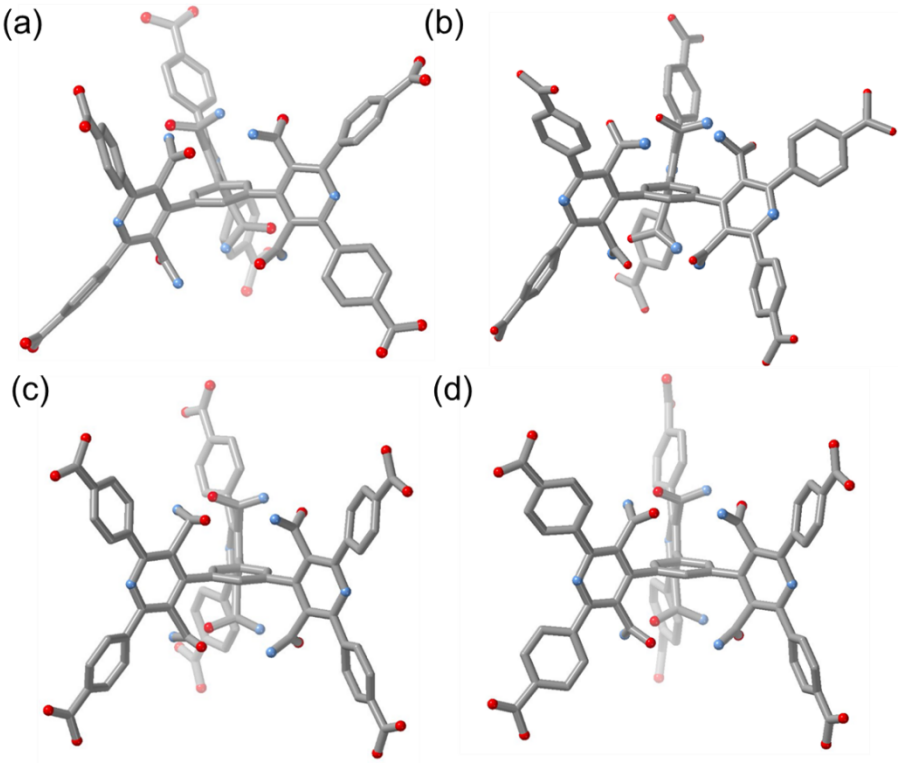

Figure S28. Comparison of torsions between DCMP arms and central benzene ring in crystal (a) solvate C1 and (b) solvate C2 and (c,d) C4.

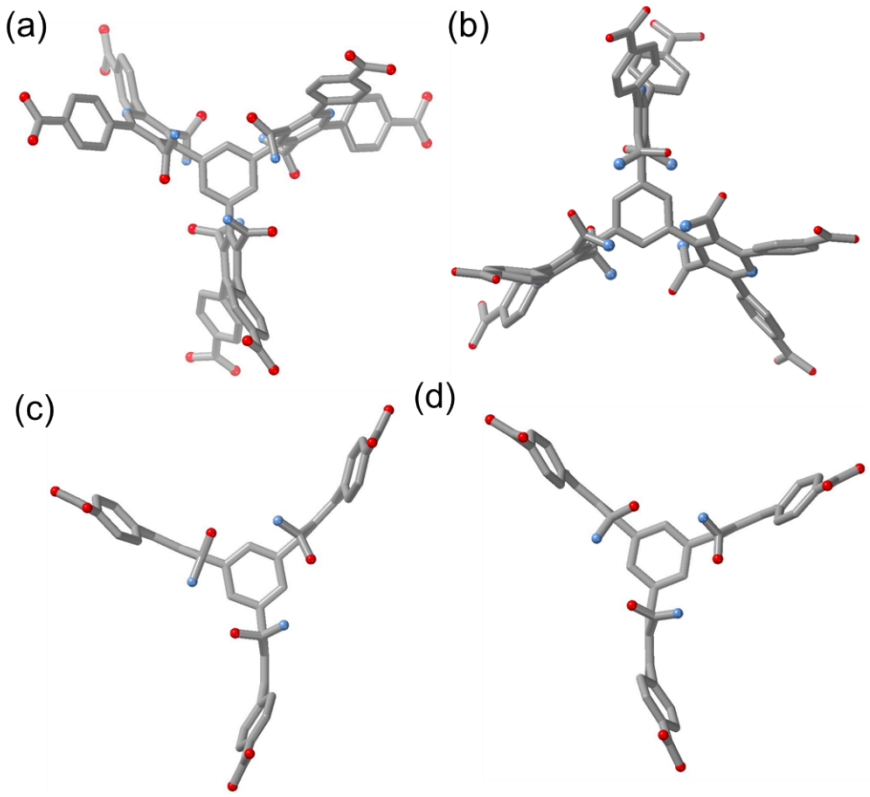

Figure S29. Comparison of torsions between DCMP arms and central benzene ring in crystal (a) solvate C1 and (b) solvate C2 and (c,d) C4. The central benzene ring is viewed as a regular hexagon.

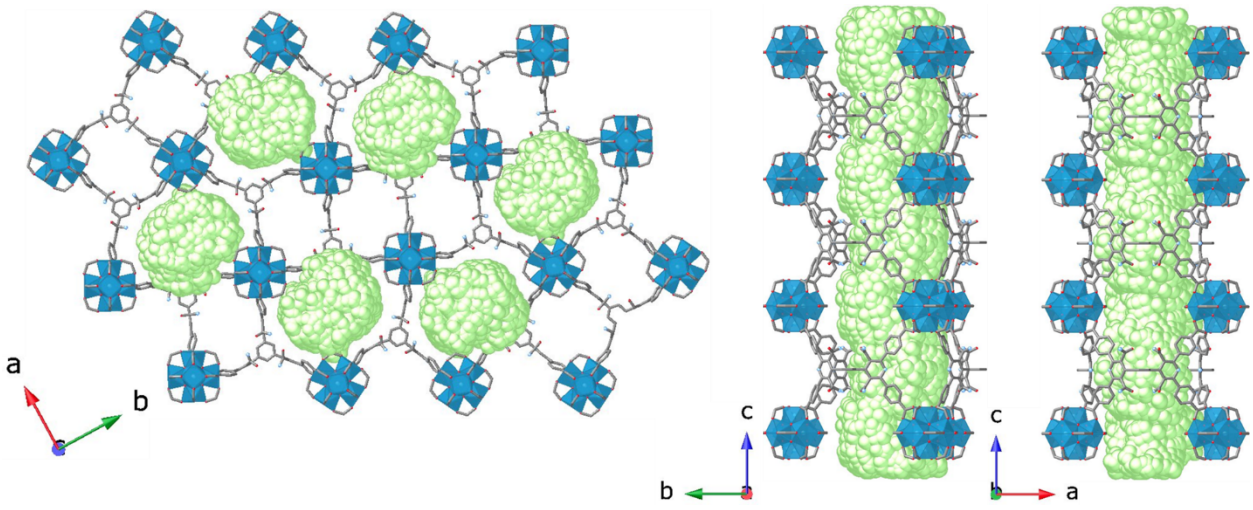

Figure S30. The distorted hexagonal-shaped 1D channels of AM-Zr-1.

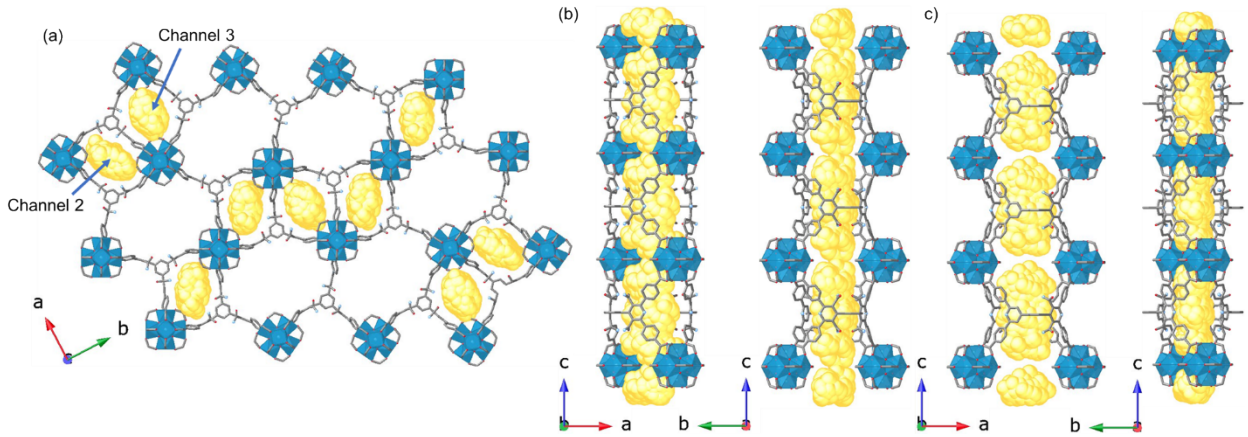

Figure S31. The two distorted small diamond-shaped 1D channels of AM-Zr-1.

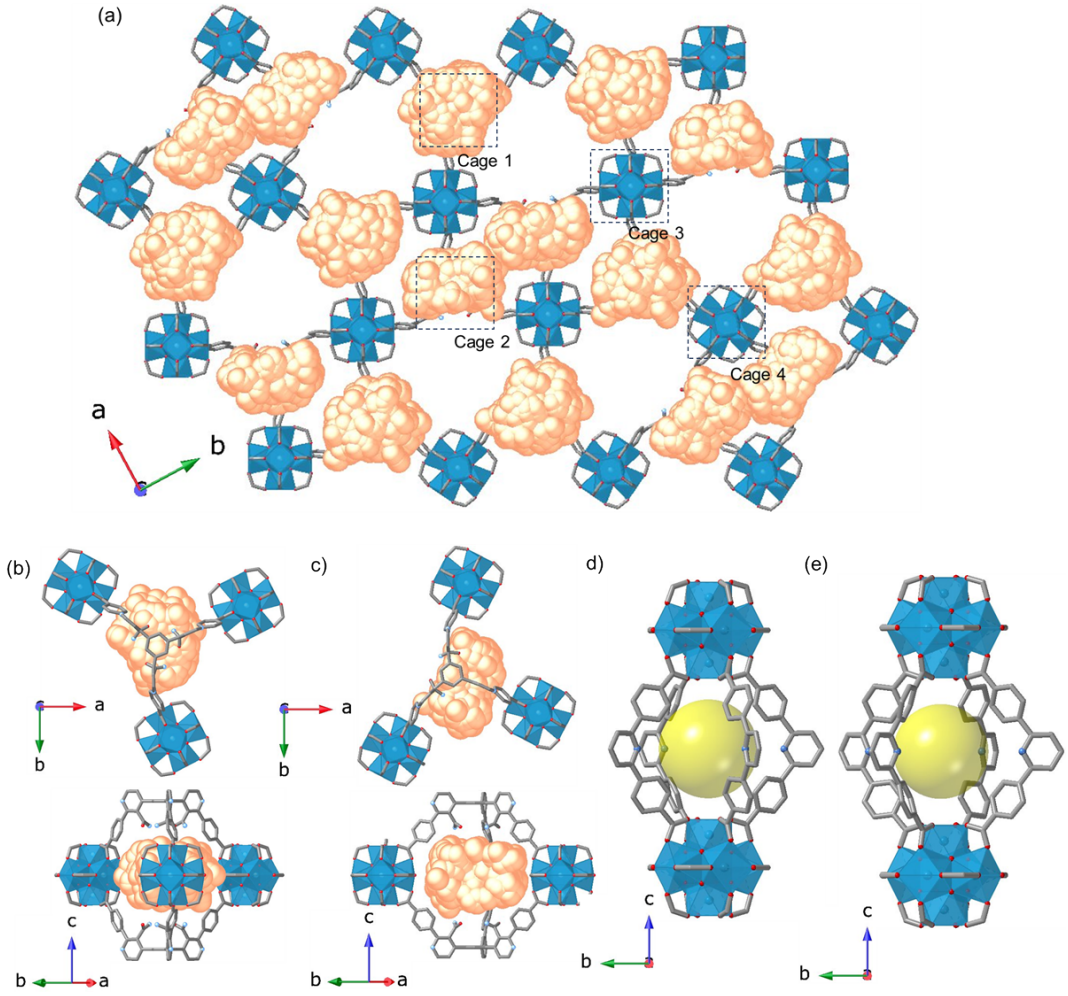

Figure S32. (a) Overview of four types of cages in AM-Zr-1. (b,c) $(Zr_6)_3$(AM-BTP)$_2$-trigonal bipyramidal cages, (b) cage 1 and (c) cage 2. The separations between the three centroids of the Zr node centers are 18.24, 20.03, and 21.29 Å for cage 1, and 18.25, 22.27, and 18.24 Å for cage 2, respectively. The distance between two central benzene ring centers is 17.73 Å. (d,e) $(Zr_6)_2$(AM-BTP)$_4$ tetragonal bipyramid cage, (d) cage 3 and (e) cage 4. The separations between

four neighbouring DCMP ring centers are 9.76 and 11.09 Å for cage 3, and 9.78, 9.99, 10.05, and 11.84 Å for cage 4, respectively. The distance between two centroids of the Zr node centers is 17.73 Å.

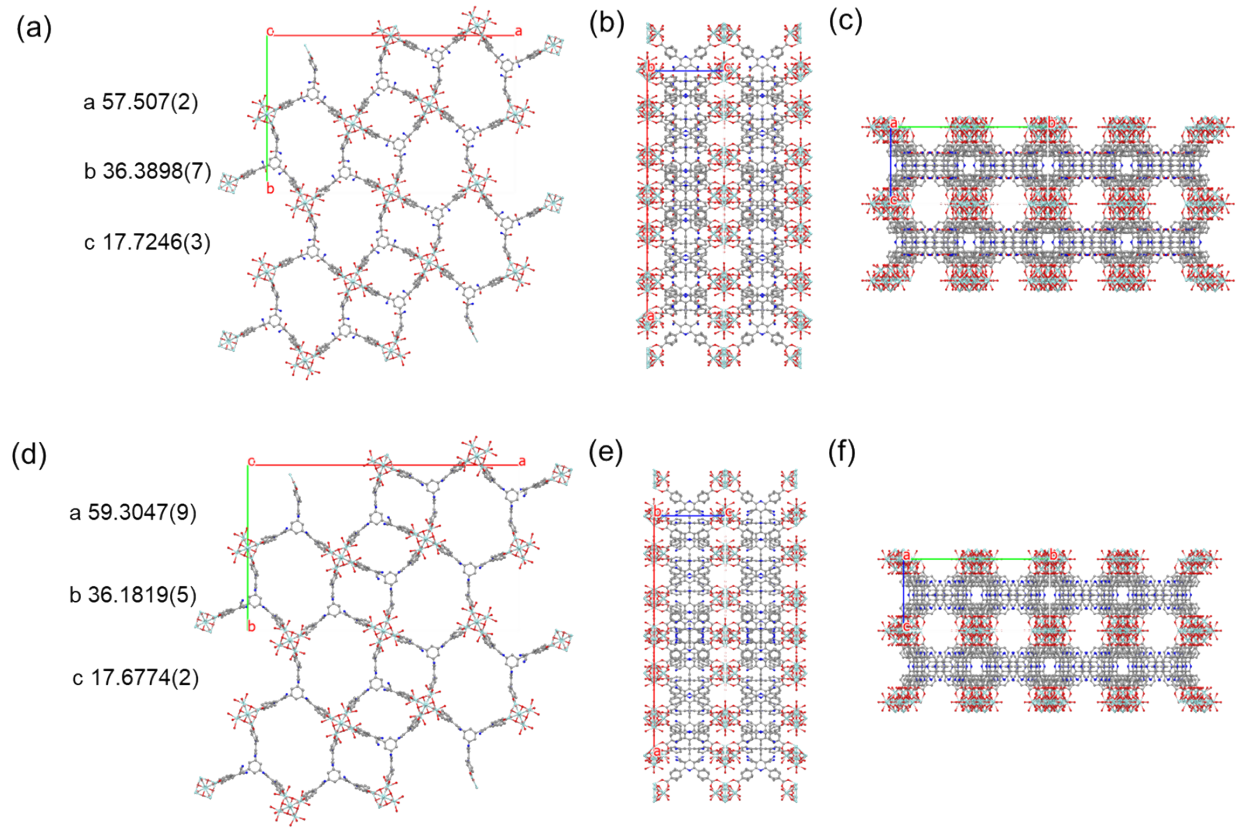

Figure S33. (a–c) Crystal structure of AM-Zr-1 (C4) viewed along different crystallographic directions. (d–f) Crystal structure of CN-Zr-1 (C5) viewed along different crystallographic directions.

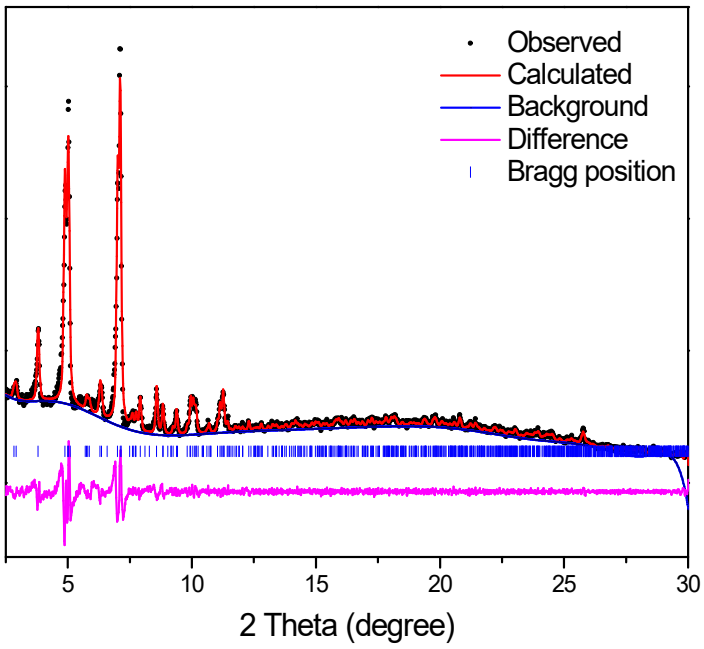

Figure S34. The structureless Le Bail refinement of the crystal structures of AM-Zr-1. The observed pattern (black line), the best Le Bail fit profile (red line), background profile (blue line), and the difference curve (purple line) between observed and calculated profiles are shown. R_{wp} = 5.994%. GoF = 2.07.

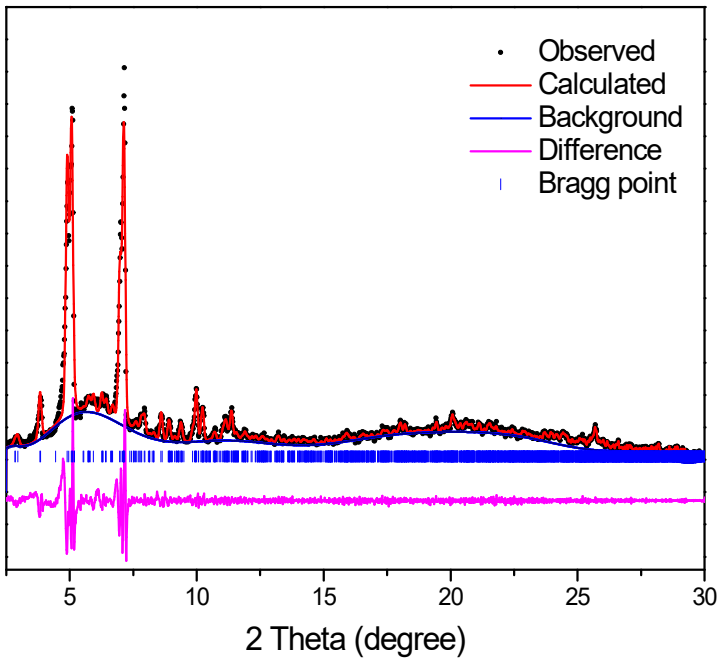

Figure S35. The structureless Le Bail refinement of the crystal structures of CN-Zr-1. The observed pattern (black line), the best Le Bail fit profile (red line), background profile (blue line), and the difference curve (purple line) between observed and calculated profiles are shown. R_{wp} = 7.41%. GoF = 2.34.

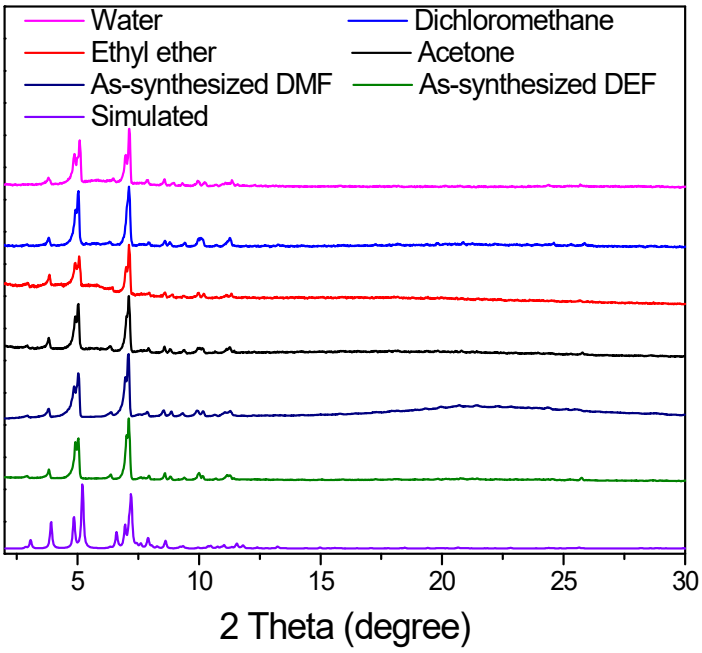

Figure S36. PXRD pattern of simulated and experimental AM-Zr-1 exchanged with various solvents.

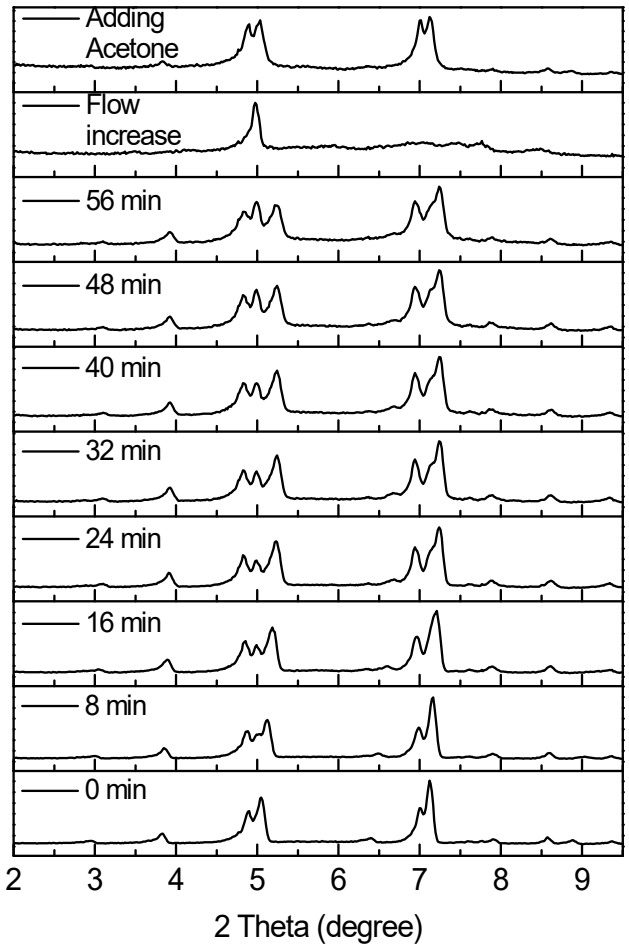

Figure S37. PXRD pattern of acetone exchanged AM-Zr-1 after flow with air for 56 min, then increasing airflow, and finally adding fresh acetone at ambient temperature.

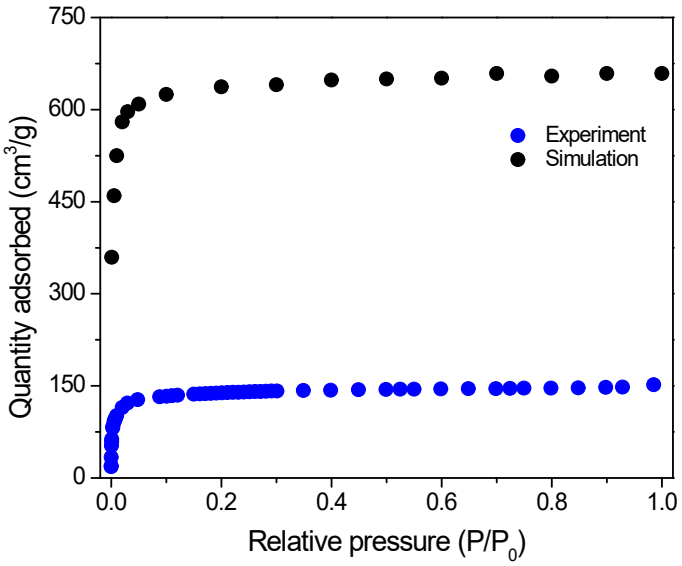

Figure S38. Simulated and experimental N_2 isotherms of AM-Zr-1 at 77 K (calculated surface area of 2660 m^2/g based on the single crystal structure of AM-Zr-1).

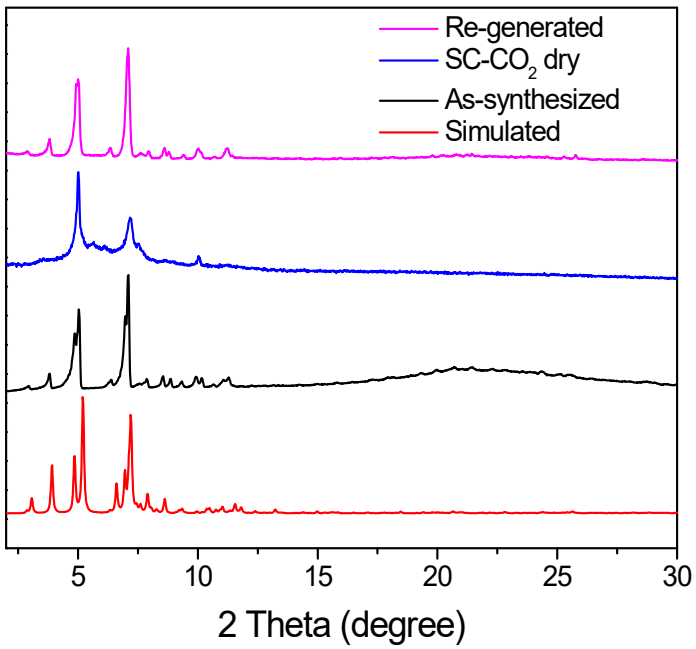

Figure S39. PXRD pattern of re-generated AM-Zr-1 compared with SC-CO_2 dried, as-synthesized, and simulated samples. The re-generated AM-Zr-1 was synthesized by using 4 mg of SC-CO_2 dried sample in 1 mL DMF and 0.4 mL formic acid at 120 ºC for 3 days.

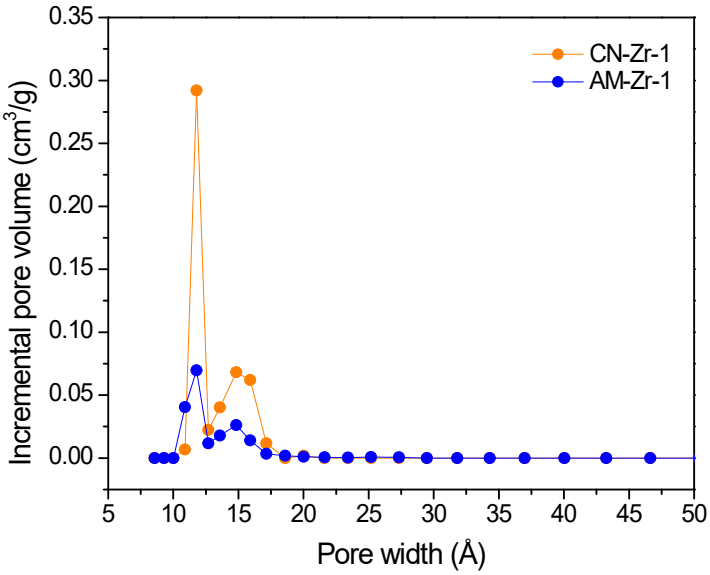

Figure S40. Pore size distributions of CN-Zr-1 and AM-Zr-1 based on a nonlocal density functional theory (NLDFT) model.

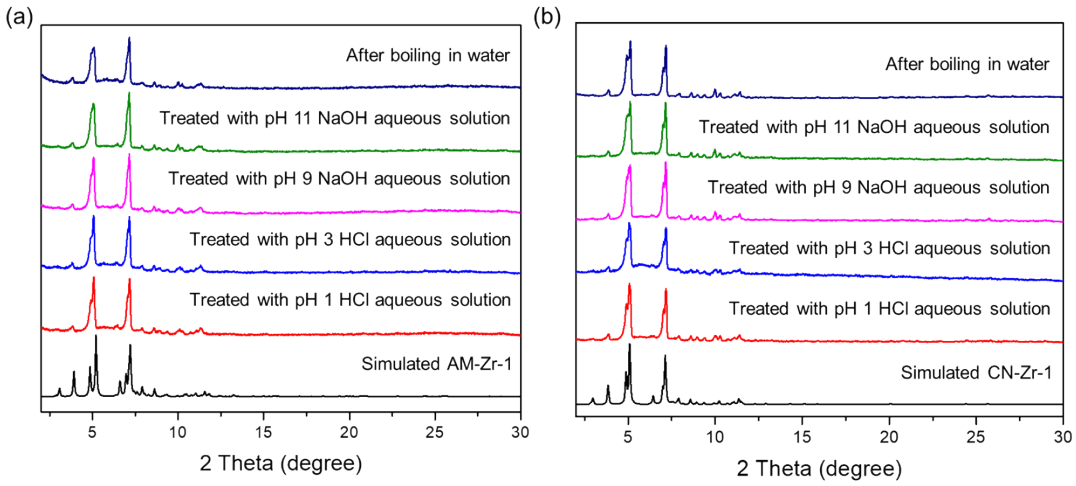

Figure S41. PXRD patterns of (a) AM-Zr-1 and (b) CN-Zr-1 after treatments with aqueous HCl and NaOH solutions, as well as after boiling in water.

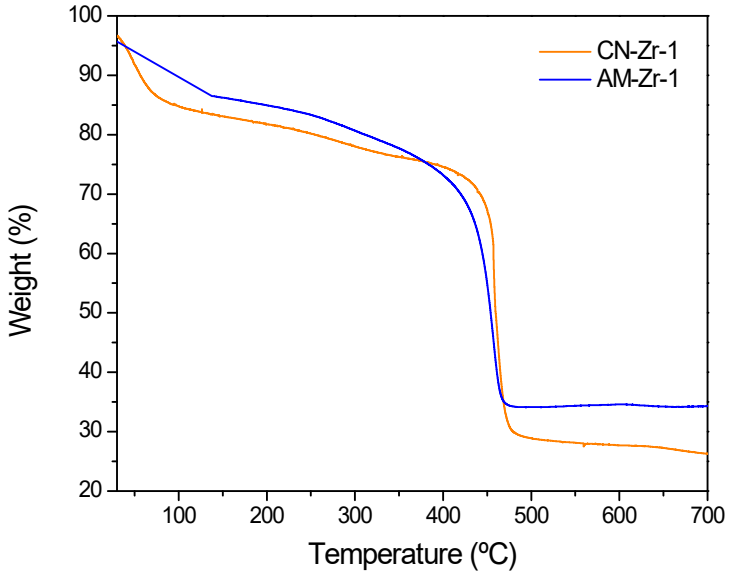

Figure S42. Thermogravimetric analyses of AM-Zr-1 and CN-Zr-1 under a nitrogen flow.

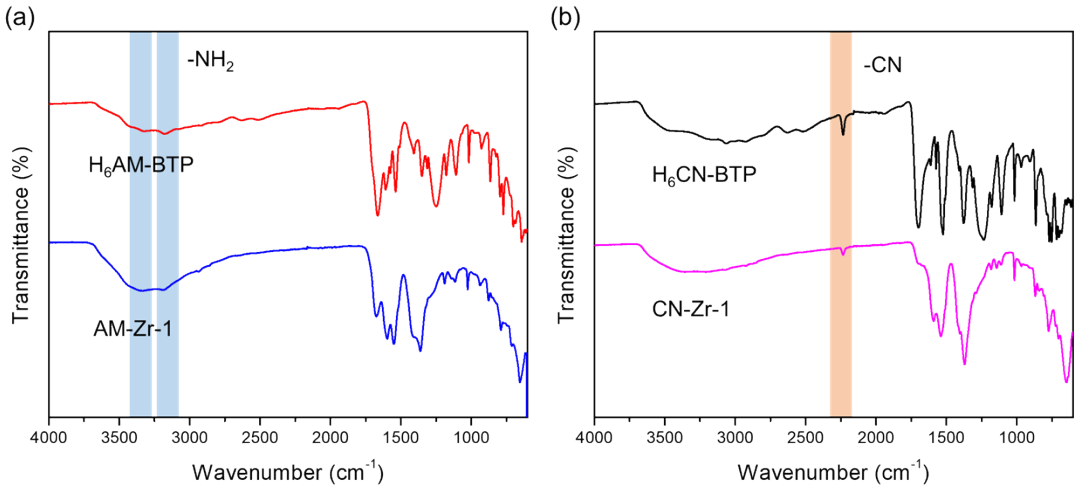

Figure S43. (a) FTIR spectra of H_6AM-BTP and AM-Zr-1. C=O stretch at around 1665 cm^{-1} and N–H stretches with two bands in 3200–3400 cm^{-1}. b) FTIR spectra of H_6CN-BTP and CN-Zr-1 with CN stretch at around 2234 cm^{-1}.

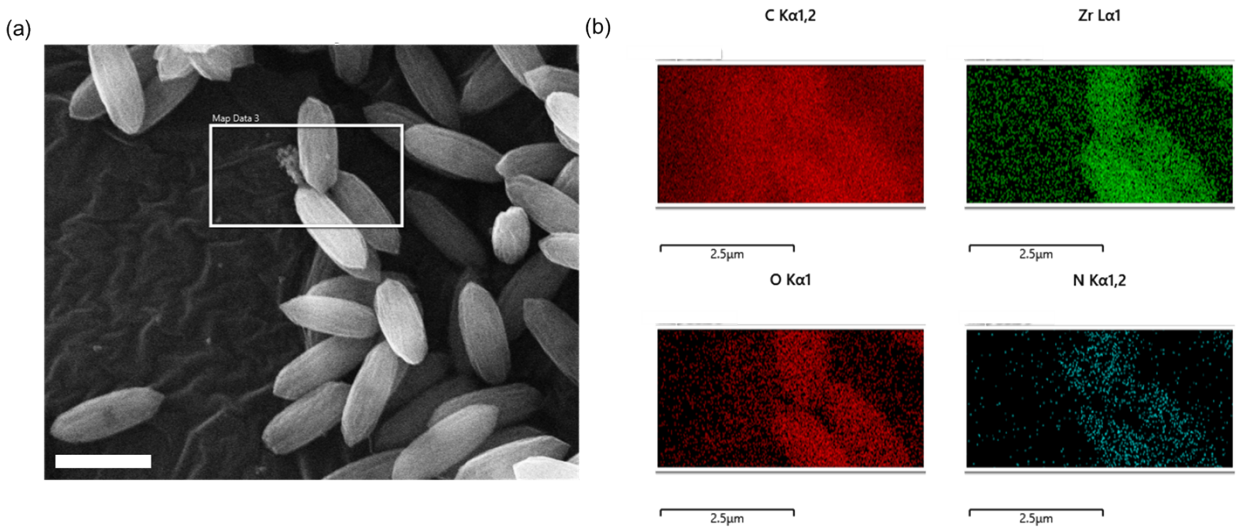

Figure S44. (a) SEM image and (b) EDS mapping of the selected area for AM-Zr-1. Scale bar = 2.5 μm.

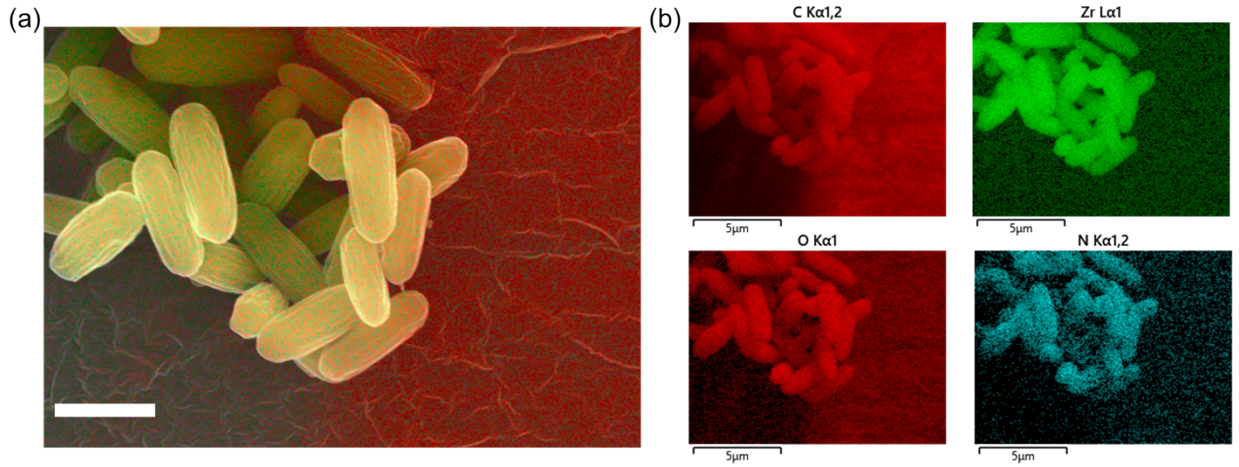

Figure S45. (a) SEM image and (b) EDS mapping of CN-Zr-1. Scale bar = 2.5 μm.

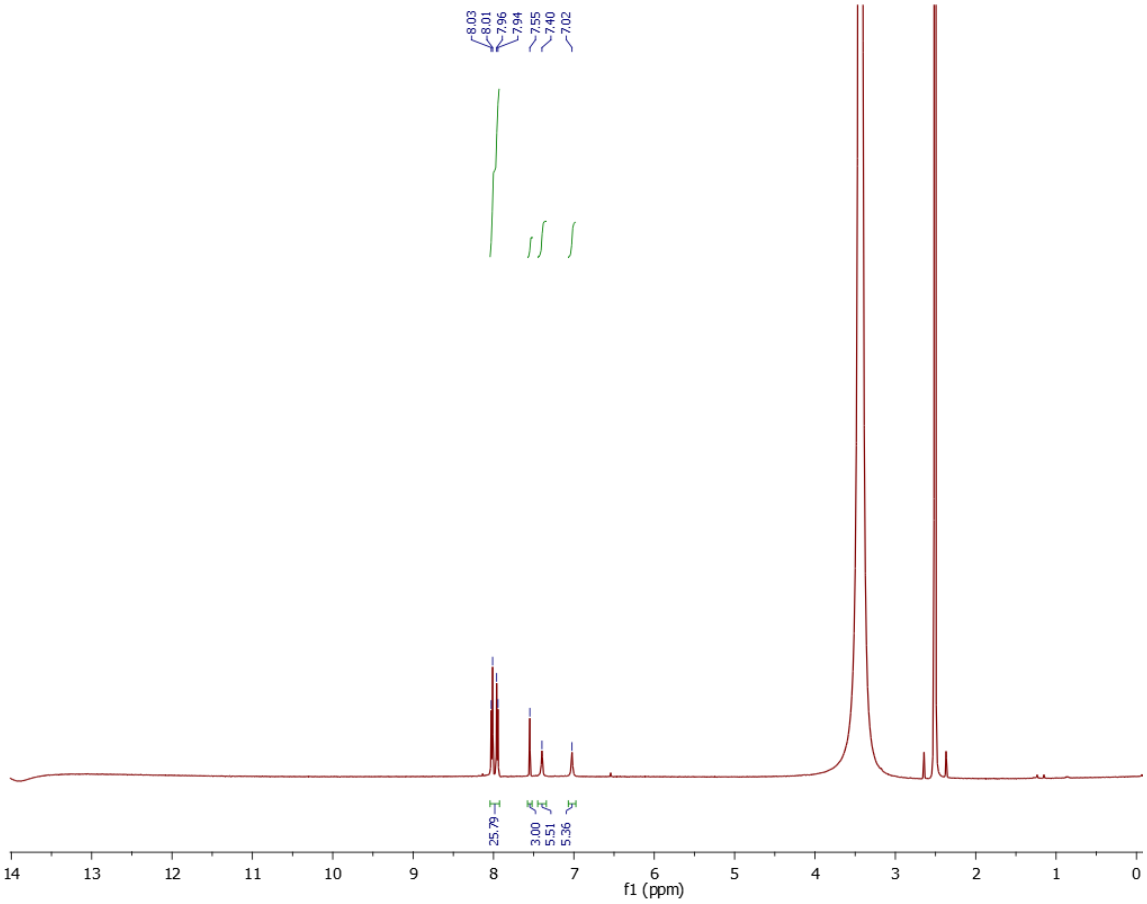

Figure S46. ^{1}H NMR spectrum of the digested AM-Zr-1 in DMSO-d_6. AM-Zr-1 powder was digested by adding 3 to 4 drops of 0.1 M NaOH aqueous solution in a vial. The vial was then capped and inverted 2 or 3 times before sonicating for 5 min. After centrifuge to remove inorganic component precipitates, the clear supernatant solution was transferred and then acidified to pH 3–5 with diluted aqueous HCl (6M). The organic solid for NMR analysis was collected and washed with water by centrifugation.

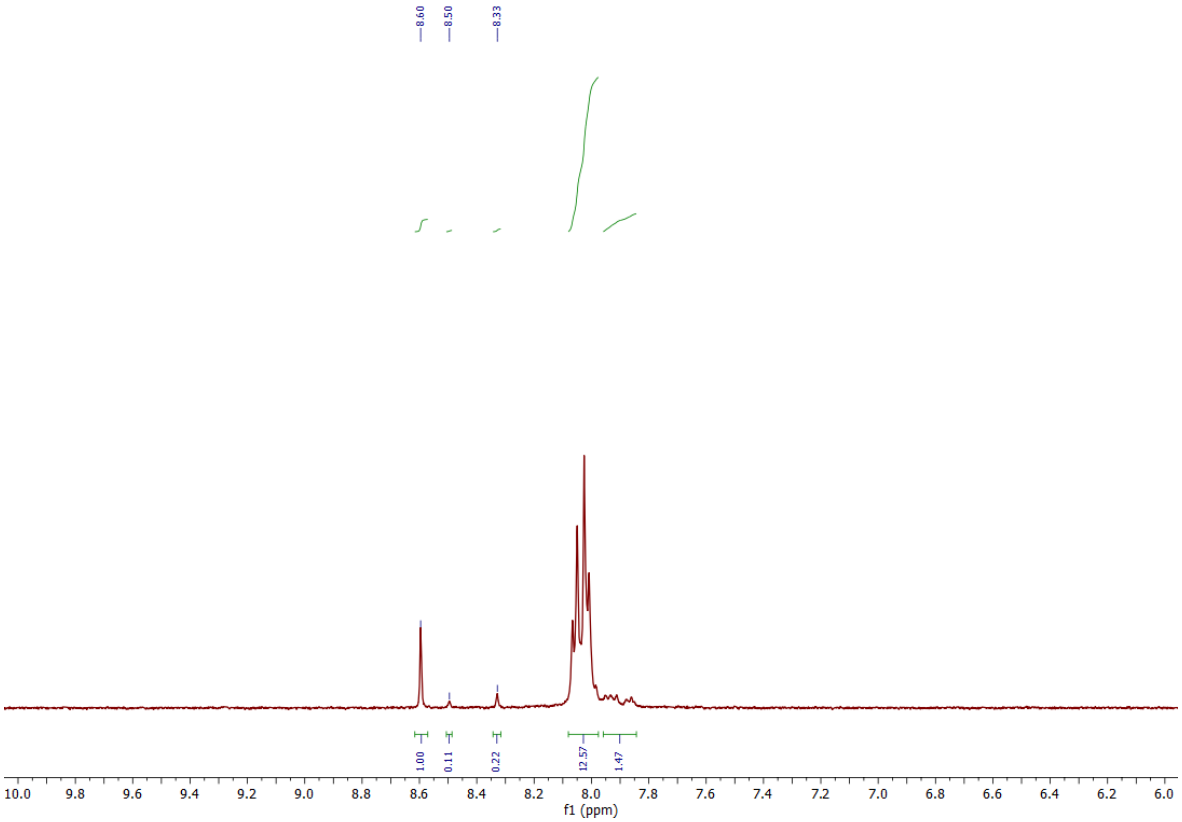

Figure S47. ^{1}H NMR spectrum of the digested CN-Zr-1 (formic acid as modulator) in DMSO-d_6. CN-Zr-1 powder was digested by adding 3 to 4 drops of D_2SO_4 solution in a vial and then diluted with DMSO-d_6. The new peaks between 8.1−8.6 ppm (8.50 and 8.33 ppm) were assigned to the central benzene protons of partially hydrolyzed H_6CN-BTP.

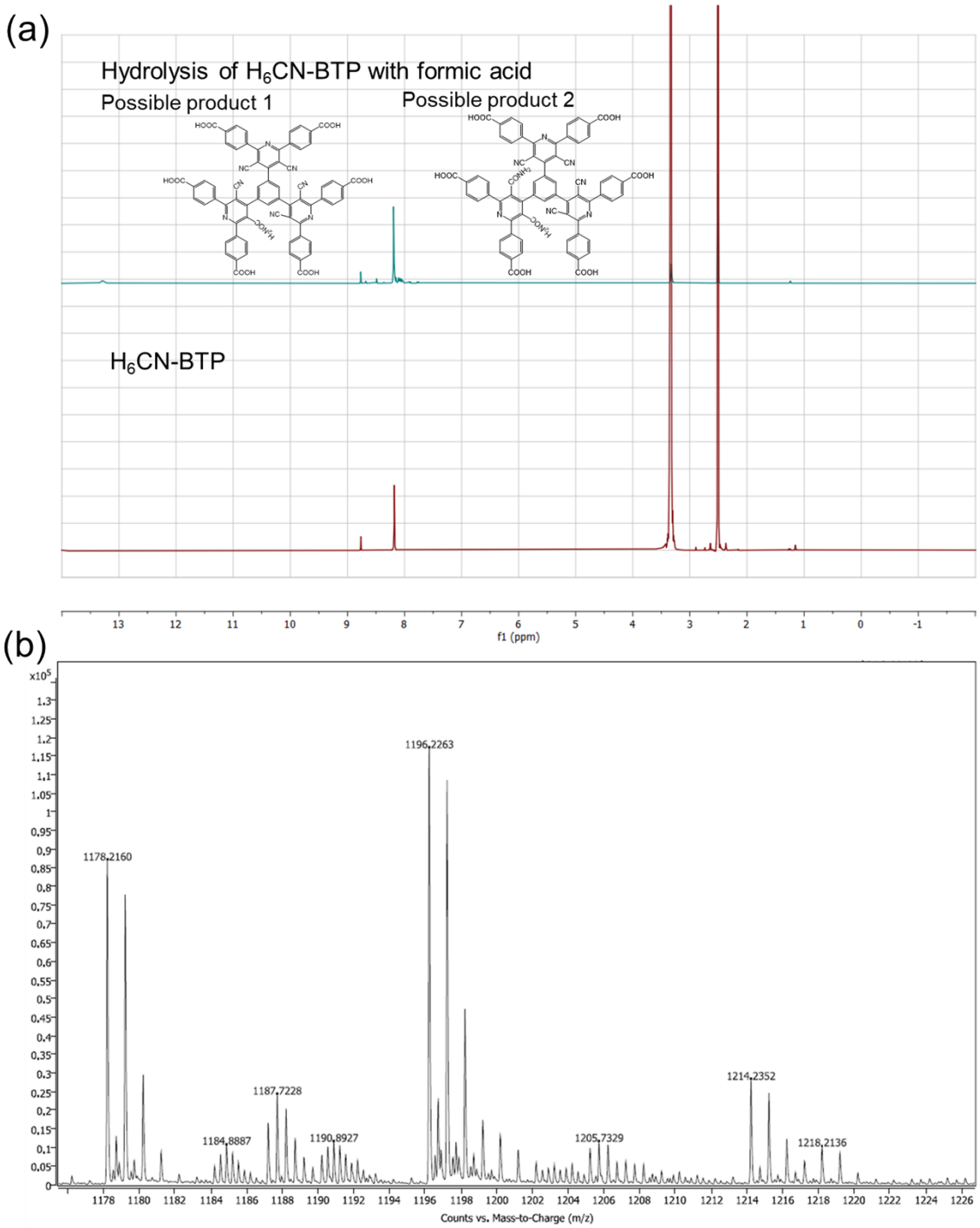

Figure S48. (a) ^{1}H NMR spectrum of hydrolyzed H_6CN-BTP with formic acid at 120 °C for 3 days and compared with H_6CN-BTP in DMSO-d_6. The new peaks were assigned to partially hydrolyzed H_6CN-BTP as confirmed by (b) MS spectrum. H_6CN-BTP: chemical formula: $C_{69}H_{33}N_9O_{12}$. HRMS (ESI, m/z): $[M-H]^-$ calculated 1178.2176; found 1178.2160. Possible product 1: chemical formula: $C_{69}H_{35}N_9O_{13}$. HRMS (ESI, m/z): $[M-H]^-$ calculated 1196.2282; found 1196.2263. Possible product 2: chemical formula: $C_{69}H_{37}N_9O_{14}$. HRMS (ESI, m/z): $[M-H]^-$ calculated 1214.2387; found 1214.2352.

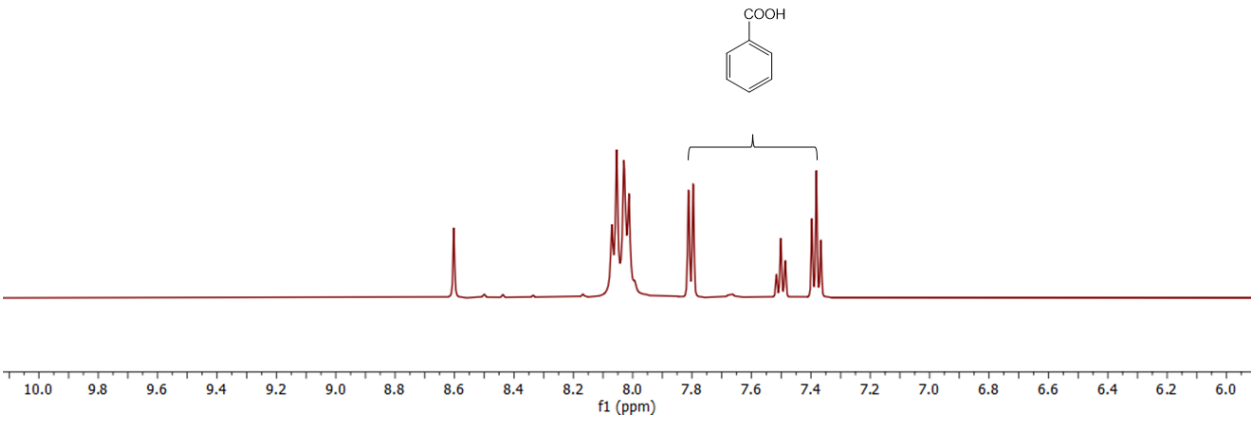

Figure S49. ^{1}H NMR spectrum of the digested single crystal of CN-Zr-1 (benzoic acid as modulator) in DMSO-d_6. CN-Zr-1 single crystal was digested by adding 3 to 4 drops of D_2SO_4 solution in a vial and then diluted with DMSO-d_6. New peaks between 8.1–8.6 ppm, assigned to protons from partially hydrolyzed H_6CN-BTP, are significantly reduced when benzoic acid is used as the modulator.

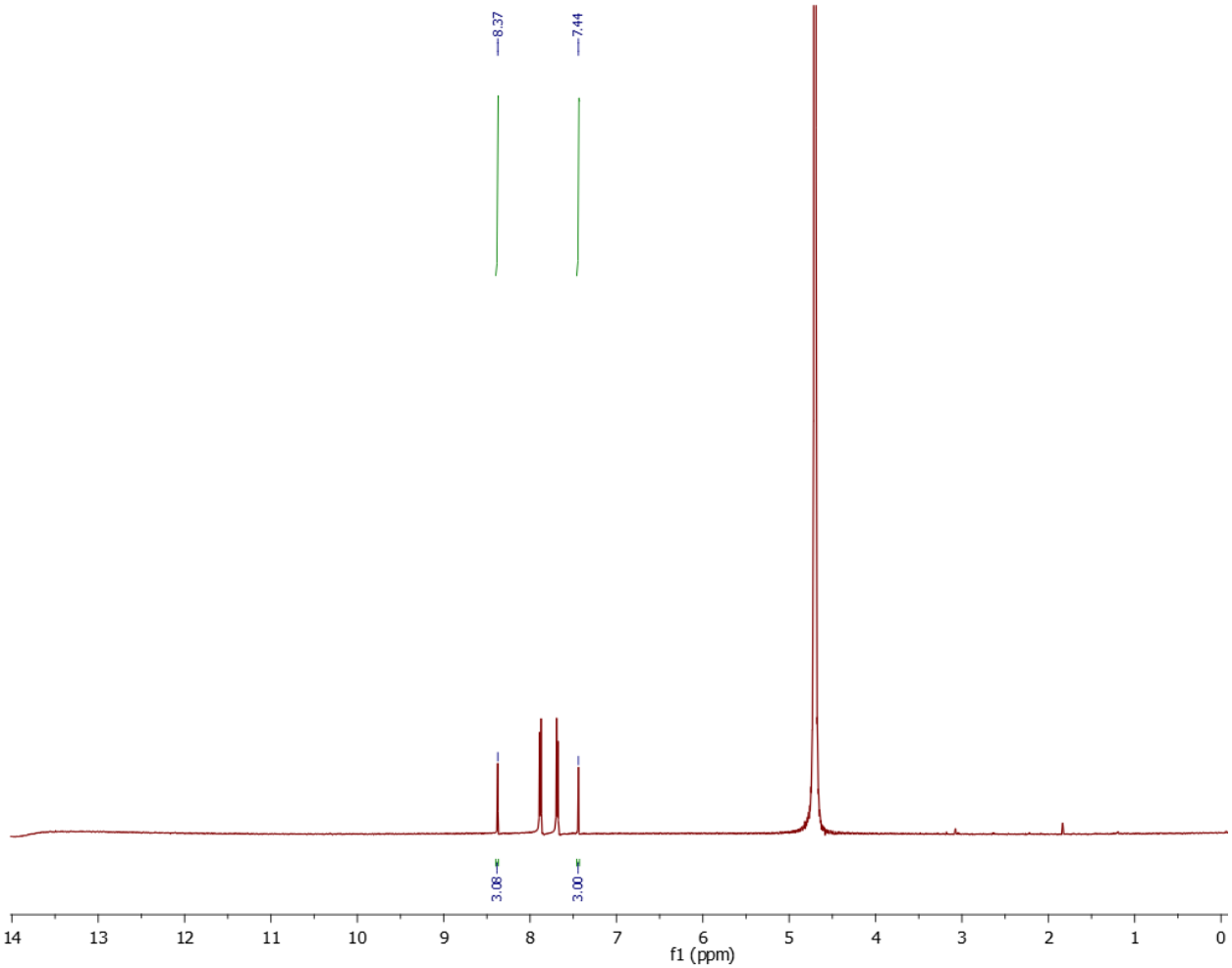

Figure S50. ^{1}H NMR spectrum of AM-Zr-1 digested in 0.1 M NaOD/D_2O and diluted in D_2O. AM-Zr-1 powder was digested by adding 3 to 4 drops of 0.1 M NaOD in D_2O in a vial. The vial was then capped and inverted 2 or 3 times before sonicating for 5 min. After centrifuge to remove inorganic component precipitates, 20 drops of D_2O were added to the clear supernatant solution, which was then transferred to NMR tube.

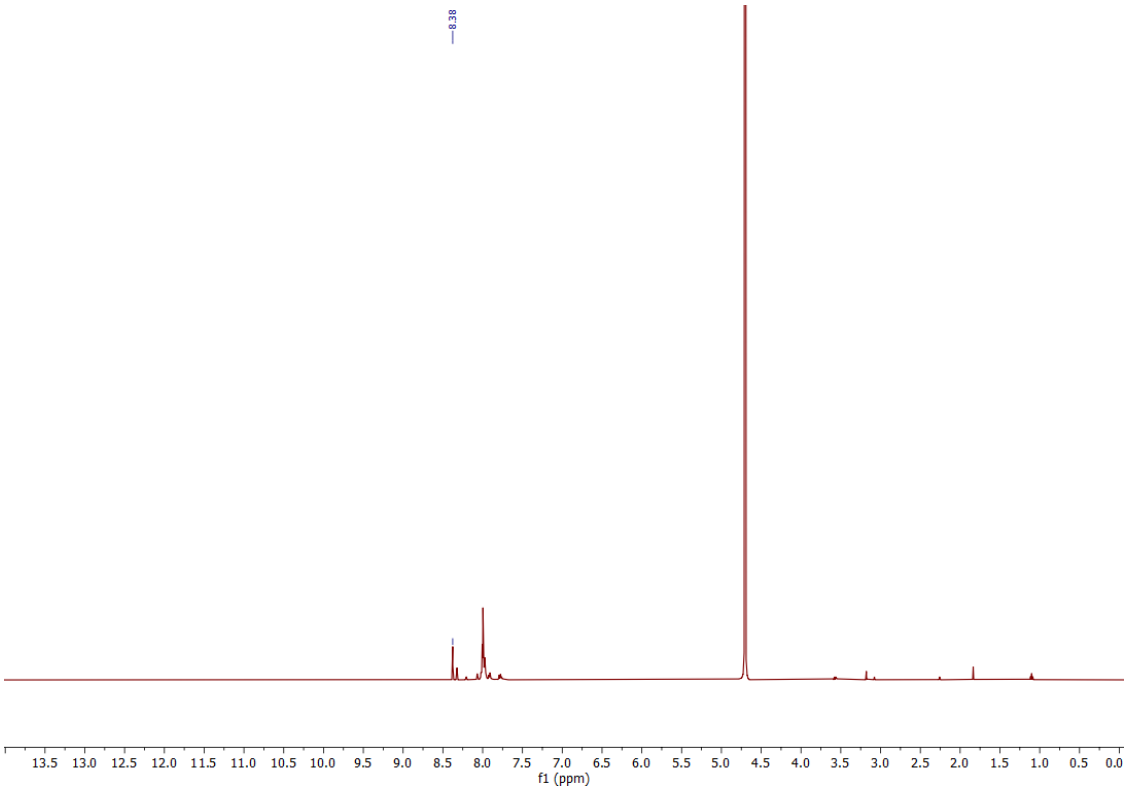

Figure S51. ^{1}H NMR spectrum of CN-Zr-1 digested in 0.1 M NaOD/D_2O and diluted in D_2O, showing the formate resonance at 8.38 ppm.

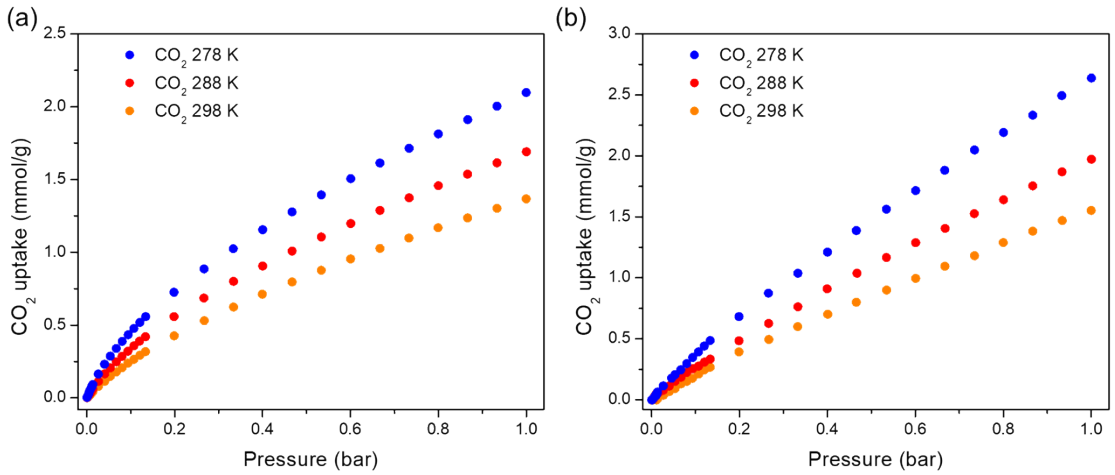

Figure S52. CO_2 adsorption isotherms for (a) AM-Zr-1 and (b) CN-Zr-1 at 278, 288, and 298 K.

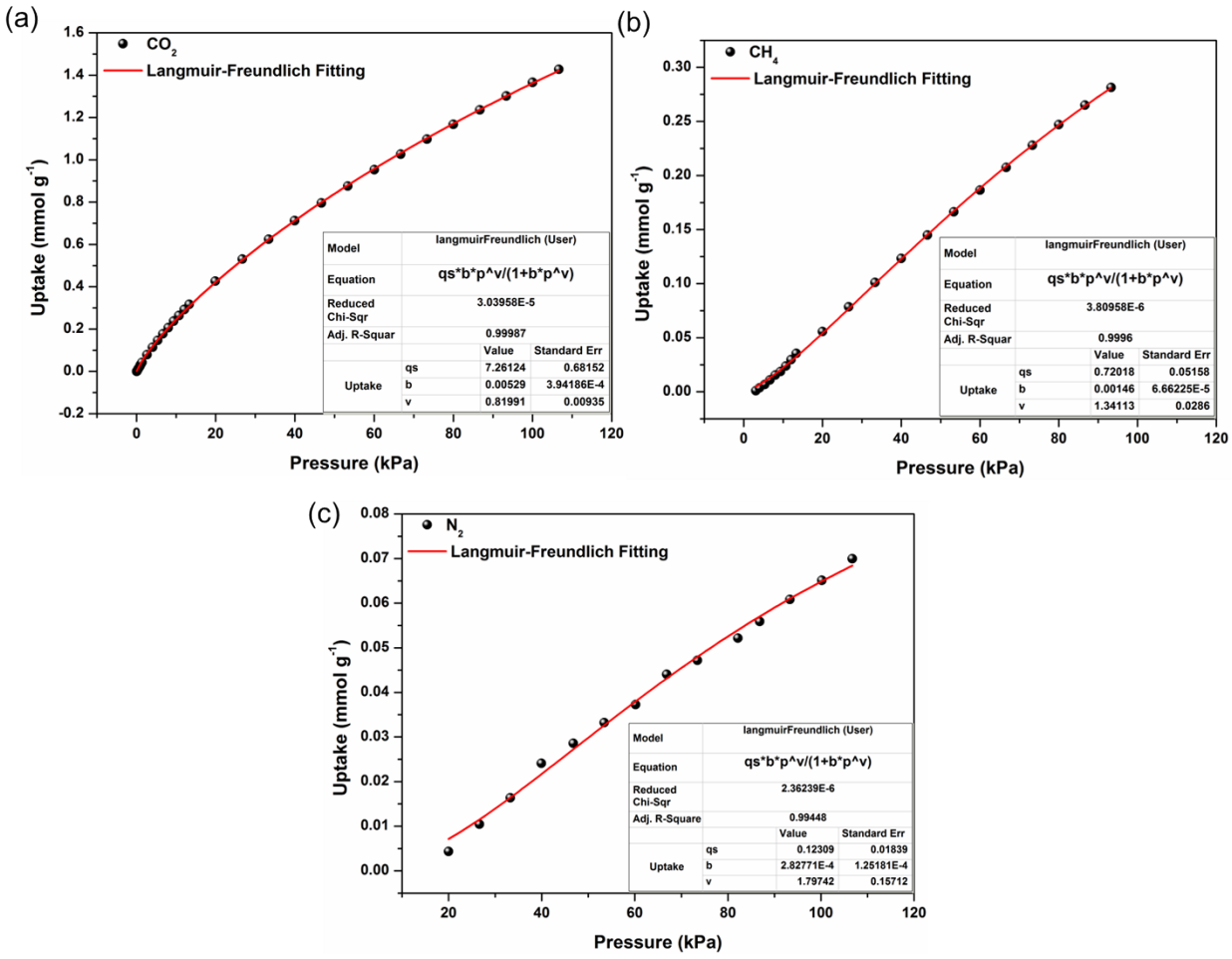

Figure S53. Fitting curve of (a) CO_2, (b) CH_4, and (c) N_2 isotherms at 298 K.

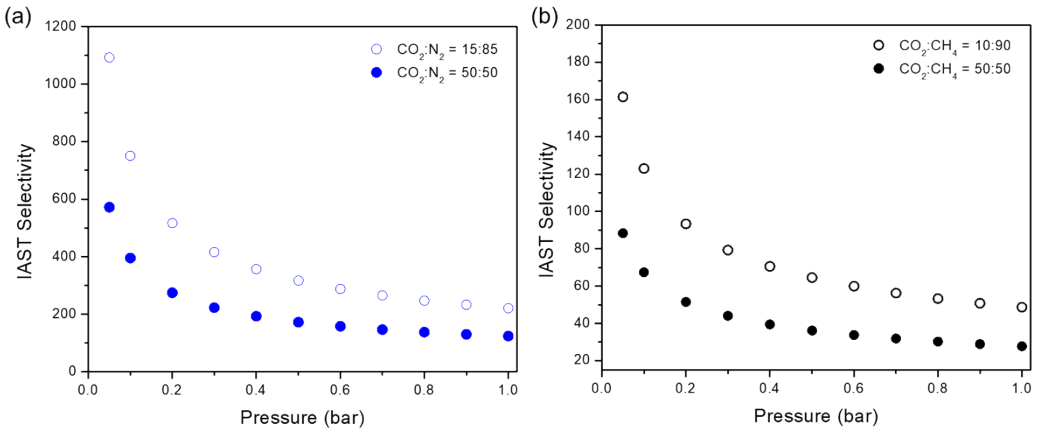

Figure S54. IAST-predicted selectivity for (a) CO_2/N_2 (15/85 and 50/50) and (b) CO_2/CH_4 (10/90 and 50/50) mixtures of AM-Zr-1 at 298 K.

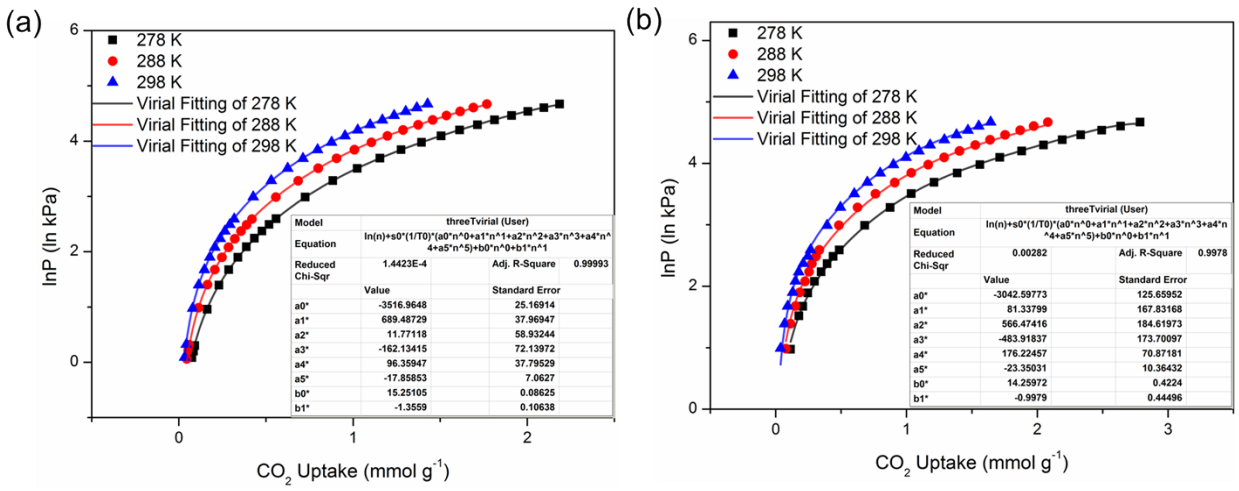

Figure S55. Fitting curve of CO_2 isotherms of (a) AM-Zr-1 and (b) CN-Zr-1 at 278, 288, and 298 K.

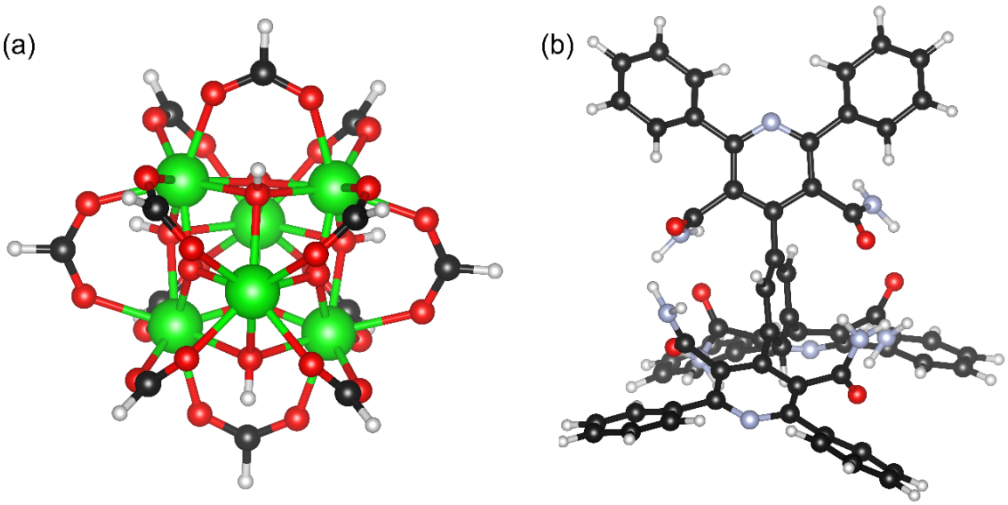

Figure S56. Optimized cluster of (a) Zr node with formate capping and (b) organic linker at M06-L+D3/Def2-TZVP level of theory. Color code: H, white; C, black; N, light blue; O, red; Zr, green. For the organic linker, the carboxylate groups were replaced with H atoms to reduce the computational cost.

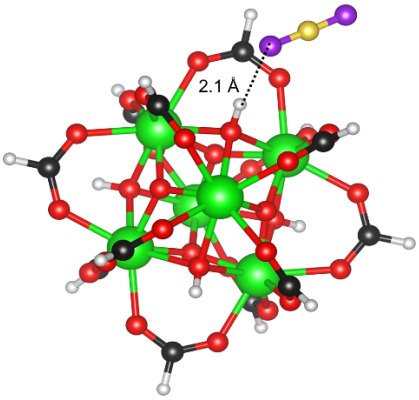

Figure S57: The lowest energy configurations of a CO_2 molecule interacting with the Zr node from DFT at the M06-L+D3/Def2-TZVP level of theory. Color code: H, white; C, black; O, red; Zr, green; C (CO_2), yellow; O (CO_2), purple.

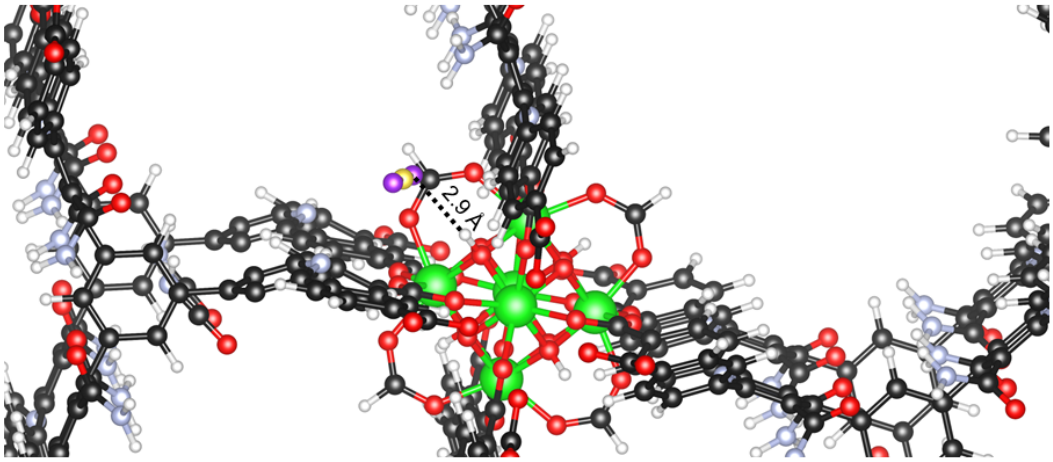

Figure S58. Optimized position of CO_2 molecule adsorbed in the periodic model using classical minimization. Using this configuration, we calculated the dispersion correction using single-point periodic DFT calculations. The dispersion correction derived from the periodic model is defined as the difference in dispersion energy between the MOF + CO_2 system and the sum of the individual dispersion energies of the MOF and the CO_2 molecule. Color code: H, white; C (MOF), black; N, light blue; O (MOF), red; Zr, green; C (CO_2): yellow; O (CO_2): purple.

Table S1. Crystal data and structure refinements.

Identification Code	C1	C2	C3	C4 (AM-Zr-1)	C5 (CN-Zr-1)
Empirical formula	$C_{93}H_{99}N_{15}O_{24}$	$C_{71}H_{61}N_9O_{26}$	$C_{71}H_{37}N_9O_{14}$	$C_{138}H_{78}N_{18}O_{60}Zr_9$	$C_{138}H_{76}N_{18}O_{48}Zr_9$
Formula weight	1810.87	1456.28	1240.09	3769.16	3575.14
Temperature / K	166(2)	225.00	250.00(10)	225.15	250.00(10)
Crystal system	triclinic	triclinic	triclinic	orthorhombic	orthorhombic
Space group	P-1	P-1	P-1	Pbam	Pbam
a / Å, b / Å, c / Å	13.93210(10), 14.43270(10), 28.2690(3)	14.7352(6), 17.8655(4), 18.0813(11)	11.6558(7), 14.5213(9), 23.5147(8)	57.507(2), 36.3898(7), 17.7246(3)	59.3047(9), 36.1819(5), 17.6774(2)
α/°, β/°, γ/°	88.3070(10), 87.3970(10), 81.9810(10)	76.095(4), 73.866(5), 78.089(3)	88.748(4), 80.115(4), 66.759(6)	90, 90, 90	90, 90, 90
Volume / Å^3	5621.33(8)	4388.4(4)	3598.1(4)	37091.7(16)	37931.4(9)
Z	2	2	2	4	4
ρ_{calc} / mg mm^{-3}	1.070	1.102	1.145	0.675	0.626
μ / mm^{-1}	0.652	0.724	0.679	2.335	2.245
F(000)	1908	1516	1276	7488	7096
Crystal size / mm^3	0.636 × 0.199 × 0.053	0.108 × 0.025 × 0.009	0.188 × 0.031 × 0.022	0.143 × 0.054 × 0.028	0.143 × 0.054 × 0.028
2Θ range for data collection	6.186 to 157.242°	6.564 to 95.366°	6.634 to 95.586	7.13 to 128.334°	4.884 to 137.196°
Index ranges	-15 ≤ h ≤ 17, -18 ≤ k ≤ 18, -35 ≤ l ≤ 35	-14 ≤ h ≤ 14, -16 ≤ k ≤ 17, -17 ≤ l ≤ 17	-10 ≤ h ≤ 11, -13 ≤ k ≤ 12, -22 ≤ l ≤ 22	-67 ≤ h ≤ 55, -37 ≤ k ≤ 42, -17 ≤ l ≤ 20	-71 ≤ h ≤ 71, -43 ≤ k ≤ 43, -21 ≤ l ≤ 18
Reflections collected	233746	39623	21231	159058	350857
Independent reflections	23156[R(int) = 0.0513]	8068[R(int) = 0.1354]	6590 [R_{int} = 0.0748]	31259[R(int) = 0.1126]	36219[R(int) = 0.1375]
Data/restraints/ parameters	23156/77/1272	8068/2270/1038	6590/2/858	31259/1494/1226	36219/1539/1189
Goodness-of-fit on F^2	1.044	1.034	1.031	1.061	1.480
Final R indexes [I>2σ(I)]	R1 = 0.0650, wR_2 = 0.1857	R_1 = 0.1234, wR_2 = 0.3447	R_1 = 0.0792, wR_2 = 0.2255	R_1 = 0.0865, wR_2 = 0.2476	R_1 = 0.1329, wR_2 = 0.3898
Final R	R1 = 0.0683,	R_1 = 0.1534,	R_1 = 0.1058,	R_1 = 0.1087,	R_1 = 0.1387,

indexes [all data]	wR_2 = 0.1884	wR_2 = 0.3737	wR_2 = 0.2488	wR_2 = 0.2661	wR_2 = 0.3962
Largest diff. peak/hole / e $Å^{-3}$	0.511/-0.451	0.599/-0.428	0.45/-0.30	1.500/-1.012	2.965/-1.941
CCDC	2454895	2454894	2486952	2454893	2504783

References

1. O. K. Farha, A. Özgür Yazaydın, I. Eryazici, C. D. Malliakas, B. G. Hauser, M. G. Kanatzidis, S. T. Nguyen, R. Q. Snurr and J. T. Hupp, *Nature Chemistry*, 2010, **2**, 944-948.
2. O. V. Dolomanov, L. J. Bourhis, R. J. Gildea, J. A. Howard and H. Puschmann, *Journal of Applied Crystallography*, 2009, **42**, 339-341.
3. G. M. Sheldrick, *Acta Crystallographica Section C: Structural Chemistry*, 2015, **71**, 3-8.
4. G. M. Sheldrick, *Acta Crystallographica Section A: Foundations of Crystallography*, 2008, **64**, 112-122.
5. A. Thorn, B. Dittrich and G. M. Sheldrick, *Acta Crystallographica Section A: Foundations of Crystallography*, 2012, **68**, 448-451.
6. E. A. Henle, N. Gantzler, P. K. Thallapally, X. Z. Fern and C. M. Simon, *Journal of Chemical Information and Modeling*, 2022, **62**, 423-432.
7. N. Planas, J. E. Mondloch, S. Tussupbayev, J. Borycz, L. Gagliardi, J. T. Hupp, O. K. Farha and C. J. Cramer, *The Journal of Physical Chemistry Letters*, 2014, **5**, 3716-3723.
8. M. J. T. Frisch, G. W.; Schlegel, H. B.; Scuseria, G. E.; Robb, M. A.; Cheeseman, J. R.; Scalmani, G.; Barone, V.; Petersson, G. A.; Nakatsuji, H.; Li, X.; Caricato, M.; Marenich, A. V.; Bloino, J.; Janesko, B. G.; Gomperts, R.; Mennucci, B.; Hratchian, H. P.; Ortiz, J. V.; Izmaylov, A. F.; Sonnenberg, J. L.; Williams; Ding, F.; Lipparini, F.; Egidi, F.; Goings, J.; Peng, B.; Petrone, A.; Henderson, T.; Ranasinghe, D.; Zakrzewski, V. G.; Gao, J.; Rega, N.; Zheng, G.; Liang, W.; Hada, M.; Ehara, M.; Toyota, K.; Fukuda, R.; Hasegawa, J.; Ishida, M.; Nakajima, T.; Honda, Y.; Kitao, O.; Nakai, H.; Vreven, T.; Throssell, K.; Montgomery Jr., J. A.; Peralta, J. E.; Ogliaro, F.; Bearpark, M. J.; Heyd, J. J.; Brothers, E. N.; Kudin, K. N.; Staroverov, V. N.; Keith, T. A.; Kobayashi, R.; Normand, J.; Raghavachari, K.; Rendell, A. P.; Burant, J. C.; Iyengar, S. S.; Tomasi, J.; Cossi, M.; Millam, J. M.; Klene, M.; Adamo, C.; Cammi, R.; Ochterski, J. W.; Martin, R. L.; Morokuma, K.; Farkas, O.; Foresman, J. B.; Fox, D. J. Gaussian 16 Rev. C.01., 2016.
9. Y. Zhao and D. G. Truhlar, *The Journal of Chemical Physics*, 2006, **125**.
10. S. Grimme, S. Ehrlich and L. Goerigk, *Journal of Computational Chemistry*, 2011, **32**, 1456-1465.
11. F. Weigend, *Physical Chemistry Chemical Physics*, 2006, **8**, 1057-1065.
12. F. Weigend and R. Ahlrichs, *Physical Chemistry Chemical Physics*, 2005, **7**, 3297-3305.
13. S. F. Boys and F. Bernardi, *Molecular Physics*, 1970, **19**, 553-566.
14. B. A. De Moor, M.-F. Reyniers and G. B. Marin, *Physical Chemistry Chemical Physics*, 2009, **11**, 2939-2958.
15. J. G. Vitillo and L. Gagliardi, *Inorganic Chemistry*, 2021, **60**, 11813-11824.

16. R. F. Ribeiro, A. V. Marenich, C. J. Cramer and D. G. Truhlar, *The Journal of Physical Chemistry B*, 2011, **115**, 14556-14562.
17. M. Hacene, A. Anciaux-Sedrakian, X. Rozanska, D. Klahr, T. Guignon and P. Fleurat-Lessard, *Journal of Computational Chemistry*, 2012, **33**, 2581-2589.
18. J. P. Perdew, K. Burke and M. Ernzerhof, *Physical Review Letters*, 1996, **77**, 3865.
19. D. Dubbeldam, S. Calero, D. E. Ellis and R. Q. Snurr, *Molecular Simulation*, 2016, **42**, 81-101.
20. D. Dubbeldam, R. Krishna and R. Snurr, *The Journal of Physical Chemistry C*, 2009, **113**, 19317-19327.
21. A. K. Rappé, C. J. Casewit, K. Colwell, W. A. Goddard III and W. M. Skiff, *Journal of the American Chemical Society*, 1992, **114**, 10024-10035.
22. N. Gabaldon-Limas and T. Manz, *RSC Advances*, 2016, **6**, 45727-45747.
23. T. A. Manz and N. G. Limas, *RSC Advances*, 2016, **6**, 47771-47801.
24. J. J. Potoff and J. I. Siepmann, *AIChE journal*, 2001, **47**, 1676-1682.
25. M. Pinheiro, R. L. Martin, C. H. Rycroft, A. Jones, E. Iglesia and M. Haranczyk, *Journal of Molecular Graphics and Modelling*, 2013, **44**, 208-219.
26. S. Parashar and A. V. Neimark, *Journal of Chemical Information and Modeling*, 2024, **64**, 3260-3268.
27. A. Nuhnen and C. Janiak, *Dalton Transactions*, 2020, **49**, 10295-10307.
28. A. L. Myers and J. M. Prausnitz, *AIChE journal*, 1965, **11**, 121-127.
29. J. Jia, F. Sun, H. Ma, L. Wang, K. Cai, Z. Bian, L. Gao and G. Zhu, *Journal of Materials Chemistry A*, 2013, **1**, 10112-10115.